Acta Materialia 262 (2024) 119440

Contents lists available at ScienceDirect

Acta Materialia

journal homepage: www.elsevier.com/locate/actamat

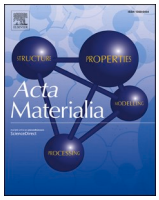

An atomistic-to-microscale characterization of the kink-controlled dislocation dynamics in bcc metals through finite-temperature coarse-grained atomistic simulations

Rigelesaiyin Ji [a], Thanh Phan [a,b], Youping Chen [c], David L. McDowell [d,e], Liming Xiong [a,b,*]

[a] Department of Aerospace Engineering, Iowa State University, Ames, IA 50011, United States
[b] Department of Mechanical and Aerospace Engineering, NC State University, Raleigh, NC 27695, United States
[c] Department of Mechanical and Aerospace Engineering, University of Florida, Gainesville, FL 32611, United States
[d] School of Materials Science and Engineering, Georgia Institute of Technology, Atlanta, GA 30332, United States
[e] G.W. Woodruff School of Mechanical Engineering, Georgia Institute of Technology, Atlanta, GA 30332, United States

ARTICLE INFO

Keywords:
Kink
Dislocation mobility
Atomistic and multiscale simulations
Stress
Temperature

ABSTRACT

Adopting bcc tungsten (W) as a model material, we characterize the temperature and stress dependence of kink dynamics on a dislocation line with length L ranging from 60 nm to 1 μm using finite-temperature coarse-grained (FT-CG) atomistic simulations. The main novelty of this work is to accommodate major salient aspects, namely the motion of μm-long dislocation lines, the atomic-scale kink dynamics, and the full spectrum of phonon dynamics, all in one single FT-CG model. At a fraction of the cost of molecular dynamics (MD) calculations, the FT-CG simulation predicts: **(a)** a dislocation-induced degeneration of the phonon density of states (PDoS) of W; **(b)** the kink-induced dislocation core structure transition from a "soft" (non-planar, compact) to a "hard" configuration (planar, split); and **(c)** the crossover from the line tension (LT) regime to the elastic interaction (EI) regime in the temperature dependence of the flow stress. Several findings arise from the simulations: **(1)** the kink activation stress, σ_f, not only depends on the temperature, T, but also exhibits a sensitivity to the dislocation line length, L. For μm-long dislocations, it approaches experimental results but σ_f for kink activation on nm-long dislocations does not; **(2)** upon an increase of T, the σ_f reduction for the sample containing μm-long dislocations is significantly larger than that for the one with nm-long dislocations; **(3)** based on data extracted from FT-CG simulations of "temperature jump tests", the L- dependence of the kink activation enthalpy, ΔH, is characterized. It can be as high as ~3 eV for a dislocation with a length of tens of nm but reduces to an experimentally comparable level of ~1.5 eV when L is 0.3 μm or longer. This suggests an easier kink activation on a longer dislocation. Such a dislocation line length dependence of ΔH can be further amplified at an even lower applied stress; **(4)** the entropic kink activation barrier, ΔH_T, is linearly proportional to T. The slope of the $\Delta H_T - T$ relation, however, will be largely underestimated in nanoscale MD simulations, but can be comparable with that from experiments when L is ~ 0.3 μm or longer. These findings highlight the limitations of nanoscale MD models in simulating kink-controlled dislocation dynamics. The knowledge gained here can support the development of mobility laws that incorporate the stress-, temperature-, and line length-dependence all into one formulation for understanding plasticity in bcc metals and other high-Peierls-stress alloys.

1. Introduction

The fundamental physics underlying plastic flow in bcc transition metals such as iron (Fe) or tungsten (W) at low temperature ($T < 0.2T_m$, T_m is the melting temperature) is not fully understood due to several inherent complexities: **(1)** plasticity is carried by screw dislocations with an average length on the order of μm [1–4] but with non-planar core structures at the nanoscale, which gives rise to a high Peierls stress (~1 GPa for Fe and ~2 GPa for W) according to density functional theory (DFT) calculations [5–10]; **(2)** these μm-long dislocation segments cannot move as a single unit due to the high Peierls barrier. Instead, their motion occurs with the aid of the thermally activated atomic-scale

* Corresponding author at: Department of Mechanical and Aerospace Engineering, NC State University, Raleigh, NC 27695, United States.
E-mail address: lxiong3@ncsu.edu (L. Xiong).

https://doi.org/10.1016/j.actamat.2023.119440
Received 11 February 2023; Received in revised form 22 September 2023; Accepted 13 October 2023
Available online 17 October 2023

kink nucleation/migration [11–16]; **(3)** although nucleated at the atomic scale, the number of the kinks and the distance that a kink travels before it interacts with another kink are sensitive to the local environment along the long dislocation line. In such scenarios, the mobility of dislocations, which governs the rate of plastic deformation of these metals, depends on the dislocation line length, in addition to conventional dependence on the stress and temperature. A mechanistic understanding of plastic flow in bcc transition metals at finite temperature demands the development of improved dislocation mobility laws that take stress-, temperature-, and line length-dependence into account. This is non-trivial, especially under the need for simultaneous consideration of the μm-long dislocation line motion along with details of atomic-level kink-pair nucleation events. Accordingly, this work focuses on developing a multi-resolution method to meet this need.

1.1. Key parameters in kink-controlled dislocation mobility laws

To understand how glide dislocations move in high-Peierls-stress materials, the theoretical formulation of the kink-controlled dislocation mobility laws has intensively attempted in the past [11–13,16–25]. Early formulations were built either upon Dorn and Rajnak's line-tension (LT) theory [11] in a low-temperature regime, or Seeger's elastic-interaction (EI) model [13] in a high-temperature regime. Such theories consider the motion of the screw dislocations to be a consequence of kink-pair nucleation and propagation along the dislocation. The resulting mobility law is furnished with two time scales together with two length scales: **(i)** the kink-pair nucleation time, t_n; **(ii)** the time (t_a, noted as its lifetime) that a kink-pair persists before it annihilates with other kinks of opposite sign; **(iii)** the distance (X, referred to as its mean free path) that a kink-pair travels before it annihilates with kinks of opposite sign; and **(iv)** the dislocation line length, L. The mobility law [15,18] according to the LT and the EI theories was written as

$$V_s = \begin{cases} v_0 h \dfrac{L}{w} \exp\left[-\dfrac{\Delta G(\boldsymbol{\sigma}, \mathrm{T})}{k_B T}\right], \text{for} t_n >> t_a \text{and} X = L, \text{LowTemperature} \\ h\sqrt{\dfrac{2v_k v_0}{w}} \exp\left[-\dfrac{\Delta G(\boldsymbol{\sigma}, \mathrm{T})}{2k_B T}\right], \text{for} t_n = t_a \text{and} X << L, \text{HighTemperature} \end{cases} \tag{1}$$

Here, V_s is the velocity of a screw dislocation segment with length L under an applied stress $\boldsymbol{\sigma}$ at temperature T; v_0 is the kink-pair nucleation attempt frequency; k_B is the Boltzmann constant; v_k is the kink velocity along the dislocation line; h and w are the kink height and width, respectively, which determine the kink activation volume ΔV; ΔG is the kink activation energy and can be written as $\Delta G = \Delta H\ (\boldsymbol{\sigma})$ - $T\,\Delta S$, where $\Delta H\ (\boldsymbol{\sigma})$ can be in a Kocks form [26] by introducing model parameters ΔH_0, T_0, p, and q. These parameters may be obtained through fitting the Kocks form into experimental data or the results from atomistic calculations, e.g., the nudged elastic band calculations in [27]. If needed, the stress ratio for capturing non-Schmid effects can be included into $\Delta H\ (\boldsymbol{\sigma})$. Clearly, one key controlling term in such kink-controlled dislocation mobility laws is ΔG and its dependence on $\boldsymbol{\sigma}$ and T. We believe one can not simply rely on DFT or classical molecular statics (MS) calculations to calibrate it because DFT and MS have a limited simulation cell at nanometer level. If a prediction of the dynamics of μm-long dislocations become desired, the parameters required by the above mobility laws need to be calibrated at the micrometer level.

1.2. Discrepancies between theories, experiments, and atomistic simulations

Given their appeal to salient physics, there is no doubt that the mobility laws in the type of Eq. (1) can yield a reasonable description of the kink-controlled dislocation dynamics for interpreting experimental observations, especially at the microscale or above [1–4]. For instance, its prediction regarding the linear line length dependence of the dislocation velocity at low temperature agrees well with the data from *in situ* straining experiments using transmission electron microscope (TEM) [1]. However, such a good correlation needs to be viewed with caution due to certain discrepancies between experiments and theories: **(1)** in experiments, the dislocation velocity is measured by tracking the screw segment of a μm-long curved dislocation with its two ends being pinned by obstacles [1] or surfaces. By contrast, Eq. (1) is formulated for a perfectly straight dislocation and does not impose any constraints on the two ends of the dislocation line [11]; **(2)** in Eq. (1), the velocity of a dislocation is formulated as a function of local stresses acting on it, which, in principle, should be a sum of the applied stress as well as the internal stress induced by its long-range interactions with other dislocations. Such a local stress, by definition, differs from the one obtained in experiments [28,29], where the local strain is directly measured and the local stress is then calculated according to certain constitutive rules, such as Hooke's law, invoking the theory of elasticity; **(3)** the mobility laws in Eq. (1) explicitly incorporate atomistic details of kinks into one formulation, including kink-pair width/height, activation enthalpy, and kink velocity. However, atomistic kink dynamics along the dislocation lines are not resolved in experiments due to limited spatial and temporal resolution. The above discrepancies highlight the limitations of many existing experimental techniques when using them to directly calibrate parameters in Eq. (1). A calibration of the mobility model and the related parameters necessitates a combination of high-fidelity simulations to be supplemented with experiments.

Over the past several decades, computational simulation has emerged as a discipline that plays a role similar to that of experiments in shedding light on complex phenomena across disparate length and time scales. Regarding kink-controlled dislocation dynamics, in contrast to first principles (e.g., DFT calculations) that have limited capability in tracking the mobile defects at finite temperature, interatomic potential-based molecular dynamics (MD) simulations have become a powerful supplement to experiments and theories. Extensive MD simulations have been performed to better understand kink-controlled dislocation motion, especially the motion of the screw dislocations in bcc Fe and W at finite temperature [14,15,20–23,27,30–39]. Despite its great success, when applied for kink-controlled dislocation dynamics in high-Peierls-stress materials, classical MD simulations are limited in the following several aspects: (1) The length of a dislocation line in a typical MD model using a modest computational resource is typically below ~100 nm, while the average lengths of the screw glide dislocations in bcc metals at low temperature, are usually ~1 μm or above [1–4]. The flow stress, which is defined here as the critical stress (σ_f) required for those μm-long dislocation line to enter the so-called kink-pair formation regime [33], may be overestimated if one only relies on nanoscale MD simulations; **(2)** there is a distribution of kink geometries when multiple kink-pairs are formed along a dislocation line. Their respective heights and widths can scatter over a broad range of $1b$ ~$5b$ (perpendicular to the dislocation line direction) and $5b$ ~$20b$ (along the dislocation line direction). Here, b is the Burgers vector. Obviously, the dislocation line (L < 100 nm) in an MD model can only accommodate a very limited number of kinks, often just a single kink pair. It may: (**a**) overestimate the kink activation volume, ΔV, by forcing an unrealistically large number of atoms on the dislocation line to participate the kinks due to the employment of the periodic boundary condition (PBC); **(b)** suppress the stochastic nature of kink-pair formation and the corresponding statistical distribution of ΔH due to a very limited number of kinks; **(c)** not exhaust all the possible modes of kink-kink interactions, e.g., cross-kink, self-pinning, or debris production. Such complicated kink dynamics on μm-long dislocation lines may significantly contribute to the dislocation mobility and then the plastic shearing rate; **(3)** the kinks on a dislocation line exert a long-range stress field [40,41] which does not fully decay to zero even at sites hundreds of nm away from the kink. Thus, the image stresses induced by the PBC or free surfaces in a nanoscale MD may give rise to spurious artifacts in estimating kink activation enthalpy, ΔH, because ΔH is believed to be highly dependent on the local stress states.

This, in turn, casts doubt on the predictive capability of mesoscale models, such as dislocation dynamics (DD) [42–49], phase field dislocation dynamics (PFDD) [50–53], or crystal plasticity finite element (CPFE) [27,54–56], if they directly accept the output from nanoscale MD to form the mobility relations in their constitutive rules. Obviously, to characterize the kink-controlled dislocation dynamics, a multiscale model is needed to bridge the length-scale gap between theories, experiments, and atomistic simulations. A fill of this gap will enable us to answer many fundamental questions, such as: (1) How does the flow stress, kink activation volume, ΔV, and the kink activation enthalpy, ΔH, depend on the dislocation line length, L? (2) What might be the minimum requirement on L in a computational model if one expects to rely on it to obtain an experimentally comparable effective values of ΔV and ΔH which are sampled over the full spectrum of kink dynamics? (3) How should we calibrate the dislocation mobility model parameters (σ_f, ΔV, and ΔH) for μm-long dislocation lines which are inaccessible to MD but dominate in experiments?

In this paper, we seek to address these questions through finite-temperature coarse-grained (FT-CG) simulations of the motion of a screw dislocation with line length ranging from several nm to ~1 μm without sacrificing the physical richness of the atomic-scale kink dynamics on the dislocation line. This approach is an extension of our previous CG model [57–63], also noted as the concurrent atomistic-continuum (CAC) method. It involves the finite element (FE) implementation of an atomistic field formulation [64–69]. This formulation is derived as an extension of the Irving-Kirkwood procedure [70–72] for unifying the atomistic and continuum description of materials within a single framework. With the interatomic potential being the only constitutive rule, and at a much lower computational cost than MD, the CG model was shown to have a unique capability of predicting the dynamics of long dislocation lines without smearing out the atomistic core structure along the lines [57–63,73–75]. Although limited previously to modeling dislocations in fcc crystals, the CG model provides us with an ideal platform that can be extended for studying the kink-controlled dislocation dynamics in bcc metals at finite temperature. In this paper, the CG model and an extension of it to FT-CG is briefly introduced in Section II. As a benchmark, the FT-CG-simulation-predicted phonon density of states (PDoS), dislocation core structure, and their comparisons with that from MD/DFT calculations are presented in Section III. Thereafter, in Section IV, we present the results from FT-CG simulations of kink dynamics on a ½<111> screw dislocation line in bcc W under a variety of stresses and temperatures. The dislocation line length dependence of σ_f, ΔV, and ΔH are analyzed in detail. The mobility model parameters in Eq. (1) as well as their dependence on L are calibrated at a length scale up to ~1 μm with the atomic-level kink dynamics on the long dislocation line being retained. In Section V, we conclude this paper with a summary of our major findings, the limitations of FT-CG, and our future endeavor.

2. Methodology

2.1. CG model for the motion of a screw dislocation in bcc metals

A numerical implementation of the atomic field formulation [69] leads to a CG model for simulating dislocation gliding in bcc crystals. Fig. 1a shows the typical set-up of a CG model which discretizes a bcc crystalline metallic sample into finite number of coarse elements. It contains a single ½<111> screw dislocation line. Each FE in the CG domain is composed of a collection of atoms. For instance, when it is embedded with 512 atoms, each FE (referred as the 512-atom FE) will have a dimension of ~1.8nm×1.8nm×1.8 nm which corresponds 8 atoms along $[1\bar{2}1]$, [111], and$[10\bar{1}]$ directions, respectively. Similarly, for 64-atom FE, it will have a dimension of ~1nm×1nm×1 nm with 4 atoms along each direction. The number of the atoms within each FE can be chosen according to the desired resolution. Through a time-integration of the equation of motion, the displacement of the atoms embedded within each node of the coarse element are explicitly solved. The atomic displacement field within the FEs is then obtained through an interpolation of the nodal displacements according to shape functions. In this work, if not specified otherwise, 512-atom FEs have been used. In this way, without the need to explicitly track the motion of each individual atom, the number of the computational degrees-of-freedom in CG is only ~0.2 % of that of a corresponding full MD simulation.

The glide of ½<111> screw dislocations within a (110) slip plane is considered as the primary carrier of the plastic flow in bcc metals at finite temperature. To accommodate the glide of this dislocation in our CG model, the shape of FE used for discretizing the sample is designed accordingly. Fig. 1b and 1c present two different FEs that can admit dislocation migration along interelement boundaries in the CG domain. The FE in Fig. 1b has a rhombohedral shape. It conforms to the dominant bcc crystal slip system by aligning its six surfaces with (110) planes. The FE in Fig. 1c is in the shape of a triangular prism. It also explicitly exposes element surfaces on (110) planes. Compared with the rhombohedral FE in Fig. 1b, such triangular prism-shaped FEs will allow a non-planar core structure, i.e., dislocation core dissociation along multiple slip planes (see more details in Section III). Moreover, distinct from traditional displacement-based finite element models (FEM), connectivity between the FEs in the CG model is not necessary in the present integral formulation. The resulting CG model thus does not involve spatial derivatives, requiring only the atomic-level internal force-displacement relation, i.e., the interatomic potential, as the sole constitutive relation. In the present work, a Proville-EAM potential for bcc W in [76] that can predict a single-humped shape of the Peierls potential along with robust {110} glide is utilized. Such a set-up ensures that both smooth and rough dislocations can migrate along the boundaries between the FEs with their surfaces aligned along the dislocation glide planes. This approach differs from many continuum approaches which accommodate dislocations using a line segment description in DD

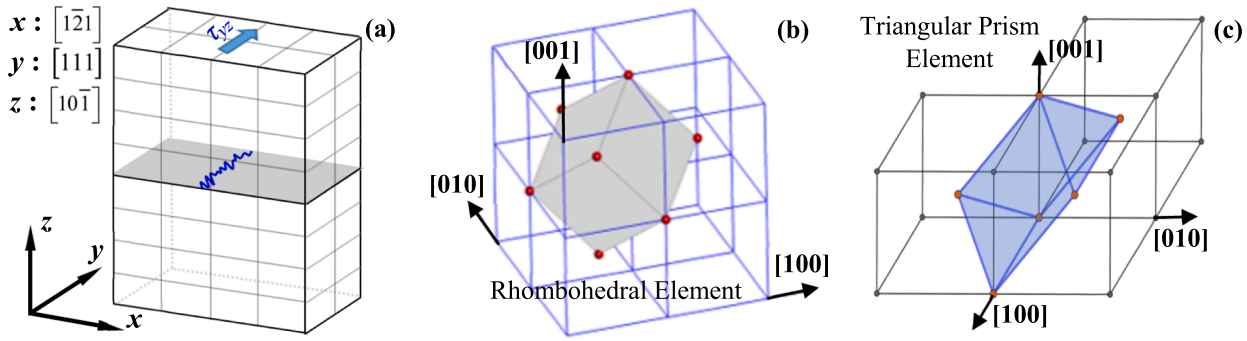

Fig. 1. The set-up of a CG model for simulating the motion of a ½<111> screw dislocation in a bcc crystal under a shear of τ_{yz}: (a) discretizing the sample into finite number of coarse FEs for simulating the dislocation (blue) gliding on a slip plane (gray); (b) the configuration of a rhombohedral element (gray) rendering its six surfaces along the (110) planes; (c) a triangular prism element with its five surfaces (light blue) being rendered along the (110) planes.

[42–49], a contact model in [77], a Heaviside step function in [78], additional degrees of freedom for the nodes of the coarse elements for slip in CPFE [54–56,79], or a complete refinement of the coarse elements down to full atomistic resolution in the quasi-continuum (QC) method [80,81]. These approaches either simply ignore the atomic-level dislocation core structures or lose the computational efficacy of a continuum model when refining down to the fully atomic scale to model the core structure. Consequently, their predictive capability and/or computational tractability will be limited when applied for characterizing the dynamics (mobility, cross-slip, etc.) of μm-long dislocations. By contrast, in our CG models, although we only solve for FE nodal displacements and do not track the motion of each atom, the FE is not the lowest level of resolution because the FEs in CG are separated from each other with a lattice constant spacing in between. Such an atomistic spacing is the lowest level of resolution. In this way, an atomistic resolution for the dislocation core is retained within the slip plane, along which the FE slide with respect to each other. This enables us to capture the dynamics of kinks with a height, h, at angstrom level. It is thus well-suited for the problem under consideration.

As a preliminary demonstration, Fig. 2 presents one snapshot from a CG simulation of the migration of a μm-long ½<111> screw dislocation within a (110) plane in bcc W under ~4 GPa at 0 K. The simulation cell is constructed with its axes along the crystallographic direction as indicated in Fig. 2a. It has a dimension of L_x = 110 nm, L_y =1000 nm, and L_z = 15 nm. This corresponds to a specimen containing ~0.1 billion atoms and is beyond the reach of a fully atomistic simulation without access to a massively parallel high performance computing resource. In this simulation, the sample is discretized into ~184,000 coarse rhombohedral FEs, each of which contains 512 atoms. A dislocation line is initially introduced into such a CG model and then driven to move until reaching a constant velocity under a shear stress of ~4 GPa. Both the dislocation line morphology and the atomic structure evolution along the line itself can be output from such CG simulations. Fig. 2a shows a snapshot of the local stress contour (τ_{yz}) on the coarse FEs within the (110) plane. The roughening of the dislocation line is clearly visible. More importantly, the dislocation line configuration can be also visualized in terms of atoms through backward mapping the atomic positions from an interpolation of the nodal positions of the coarse FEs (see the inset pictures in Fig. 2a). Surprisingly, the atomic-level roughness (height: h; width: w) along the μm-long dislocation line is captured by CG at a very high resolution (see inset picture of Fig. 2a). Also, such a CG model can even accommodate the kink formation along multiple slip planes (see Fig. 11 in a later section). To characterize the FE mesh size dependence of the dislocation line morphology, we perform CG simulations with a mesh size of 64 atoms per element (Fig. 2b) and also full MD simulations (Fig. 2c) at a temperature of 10 K. A comparison of Fig. 2a–c shows that, despite the usage of a linear shape function, the height of the atomic roughness, denoted as h, along the dislocation migration direction is nearly independent of the mesh size.

For the kink width (noted as w) along the dislocation line direction, due to the deployment of linear FE shape function, different from kink height, w does exhibit a notable FE mesh dependence: the coarse FE, the larger w. This can be evidenced by comparing Fig. 2a (512 atoms per FE) with Fig. 2b (64 atoms per FE). The FE mesh size dependence of kink

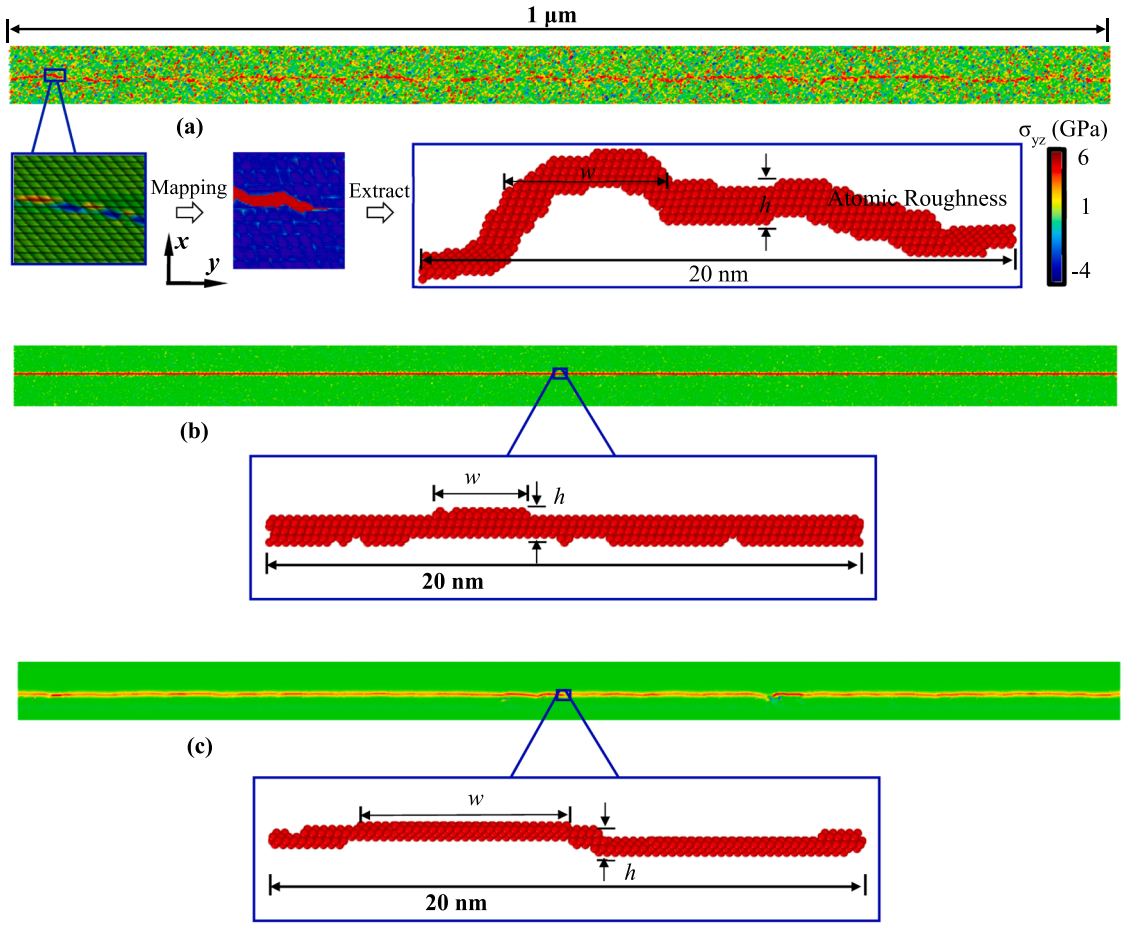

Fig. 2. A snapshot the CG-simulation-predicted rearrangement of the coarse FEs resulting from the dislocation migration within the slip plane and its comparison with that from full MD simulations at 10K: (a) results from the CG simulation where the sample is discretized into 512-atom FEs. Each FE is in a dimension of ~1.8nm×1.8nm×1.8 nm; (b) results from the CG simulation where the sample is discretized into 64-atom FEs. Each FE is in a dimension of ~1nm×1nm×1 nm; and (c) full MD simulation results.

width, however, does not mean that CG model is not applicable for characterizing the kink dynamics along the long dislocation line because: **(a)** kink activation is stochastic; **(b)** its width, w, is not a constant and ranges from several to tens of nanometers instead. This is also one reason why the kink width, w, in Fig. 2c from full MD can be even larger than that from CG in Fig. 2a, b. To confirm the applicability of our CG models in capturing the stochastic nature of w, at $T = 100$ K, we performed CG computational analysis of the distribution of kink width, w, as well as its dependence on the dislocation line length (noted as L) and shear stress (noted as τ). The relevant result and its comparison with that from full MD are shown in Fig. 3. Several main findings are: **(1)** when L is short, such as $L = 150$ nm or below, MD simulations show that w is not so sensitive to L. The dominating w is around 3 nm (Fig. 3a); **(2)** the distribution of w predicted by CG at $L = 150$ nm (Fig. 3b) is comparable with that by MD (Fig. 3a); **(3)** when L increases from 150 nm to 1000 nm, CG simulations show that w exhibits a clear dependence on L. The dominating kink width at $L = 1000$ nm is around 25 nm (Fig. 3b); **(4)** for $L = 1000$ nm, when the applied shear stress increases from 2 GPa to 4 GPa, the distribution of the kink width is largely narrowed down. The dominating kink width is $w = 25$ nm when $\tau = 2$ GPa but is only $w = 3$ nm at $\tau = 4$ GPa (Fig. 3c).

Overall, we believe our CG models reasonably predict the distribution of both the kink heights, h, at the atomic-scale and also the kink width, w. Although the CG simulation-predicted w exhibits a notable mesh size dependence (the CG model using coarser FEs will lead to a larger kink activation volume and a higher kink activation enthalpy due to such a mesh size dependence), the results can converge to the full MD simulation results in the high-temperature high-stress regime (see details in Section IV of this paper).

2.2. An extension of CG to FT-CG for kink-controlled dislocation dynamics at finite temperature

Despite the above success of modeling the dislocation motion using CG, we are aware that the thermal-induced roughening of a dislocation line needs to be appropriately included, especially when a characterization of the kink-controlled dislocation dynamics at finite temperature is desired. Our previous CG models for simulating dislocations in fcc crystals [57–63,73–75] considered systems in an equilibrium with a homogeneous temperature field, ignoring the thermal fluctuations. Hence, the kinetic stress was assumed to be a constant resulting from a homogeneous temperature field. Such a treatment precludes the thermal fluctuation-promoted kink activation along the dislocation line.

To accommodate the thermal-induced kink activation along a dislocation line in CG, we need to remove the assumption of a homogeneous temperature field and allow fluctuations. At the atomic scale, recall that temperature in the molecular kinetic theory is defined in terms of the mean kinetic energy of particle k, i.e., $\langle m_k \mathbf{v}_k^2/2\rangle = 3k_BT/2$. When the given temperatures above the Debye temperature, the equipartition theorem states that every degree of freedom has an average energy of $k_BT/2$. For monatomic crystals, the total kinetic energy of an 8-node finite element containing $n_e = V_e/V$ lattice cells can be thus written as

$$\begin{aligned} K_e &= \int_{V_e}\int\int \frac{1}{2}\sum_{k=1}^{N_l} m_k(\mathbf{v}_k)^2\delta(\mathbf{x}-\mathbf{r}_k)d^3x \\ &= \int_{V_e}\int\int \frac{1}{2}\rho\mathbf{v}^2 d^3x + \int_{V_e}\int\int \frac{1}{2}\sum_{k=1}^{N_l} m_k(\widetilde{\mathbf{v}}_k)^2\delta(\mathbf{x}-\mathbf{r}_k)d^3x \\ &= \int_{V_e}\int\int \left(k_1+k_2\right)d^3x = n_e\times(3k_BT/2). \end{aligned} \tag{2}$$

Here, k_B is the Boltzmann constant; V_e and V are the volumes of one FE and one lattice cell, k_1 and k_2 are the kinetic energy density due to the motion of FE nodes and that due to the motion of the omitted degrees of freedom, respectively; n_e is the total number of the lattice cells embedded within an element; m_k and v_k are the mass and velocity of the atom in the k-th lattice cell, respectively; δ ($\boldsymbol{x}$-$\boldsymbol{r}_k$) is the Dirac delta defined by its sifting property; $\boldsymbol{r}_k$ and $\boldsymbol{x}$ are the positions of the k-th lattice cell in phase and physical space, respectively. The balance equation of linear momentum can be then expressed as

$$\rho\dot{\mathbf{v}} = \mathbf{f}^{\text{int}}(\mathbf{x},t) - \frac{1}{V}\int_{\partial V}\sum_{k=1}^{N} m\widetilde{\mathbf{v}}_k\widetilde{\mathbf{v}}_k\delta(\mathbf{x}+\mathbf{x}^{'}-\mathbf{r}_k)\cdot\mathbf{n}d^2\boldsymbol{x}^{'} = \mathbf{f}^{\text{int}}(\mathbf{x},t) + \mathbf{f}^{T}(\mathbf{x},t) \tag{3}$$

where the $\mathbf{f}^{\text{int}}(\mathbf{x},t)$is the internal force field, which can be derived from the interatomic potential, and $\mathbf{f}^{T}(\mathbf{x},t)$is related to temperature via its time average or ensemble average, i.e.,

$$\begin{aligned} \left\langle \mathbf{f}^{T}(\mathbf{x},t)\right\rangle &= -\frac{1}{V}\left\langle \int_{\partial V}\sum_{k=1}^{N_l} m\widetilde{\mathbf{v}}_k\widetilde{\mathbf{v}}_k\delta(\mathbf{x}+\mathbf{x}^{,}-\mathbf{r}_k)\cdot\mathbf{n}d^2x^{'}\right\rangle \\ &= -\int_{\partial V}\left\langle \sum_{k=1}^{N_l} m(\widetilde{\mathbf{v}}_k)^2\delta(\mathbf{x}+\mathbf{x}^{'}-\mathbf{r}_k)\right\rangle\cdot\mathbf{n}d^2x^{'} \\ &= -2\int_{\partial V}\langle k_2(\mathbf{x}+\mathbf{x}^{'},t)\rangle\cdot\mathbf{n}d^2x^{'} = -\beta\nabla T(\mathbf{x},t), \end{aligned} \tag{4}$$

where k_2 is the density of kinetic energy due to the velocity difference$\widetilde{\mathbf{v}}_k$; the bracket in Eq. (4) represents a time or ensemble average by which the averaged function becomes smooth; β is a constant that can be determined by the resolution of the size of a finite element, with$\beta = 3(n_l - 8)k_B/V_e$for a system that is discretized via 8-node hexahedral FEs; the instantaneous $\mathbf{f}^{T}(\boldsymbol{x},t)$ can be expressed as

$$\mathbf{f}^{T}(\mathbf{x},t) = -\beta\nabla T(\mathbf{x},t) + \boldsymbol{\eta}(t) + \mathbf{f}^{D}(\mathbf{x},t), \tag{5}$$

with

$$\boldsymbol{\eta}(t) = -2\int_{\partial V}\Delta k_2\mathbf{n}d^2x^{'}\text{and}\langle\boldsymbol{\eta}(t)\rangle = 0 \tag{6}$$

where $\Delta k_2$is the deviation from the mean kinetic energy$\langle k_2\rangle$, which fluctuates around the average value, $\mathbf{f}^{D}(\boldsymbol{x},t)$accounts for the difference

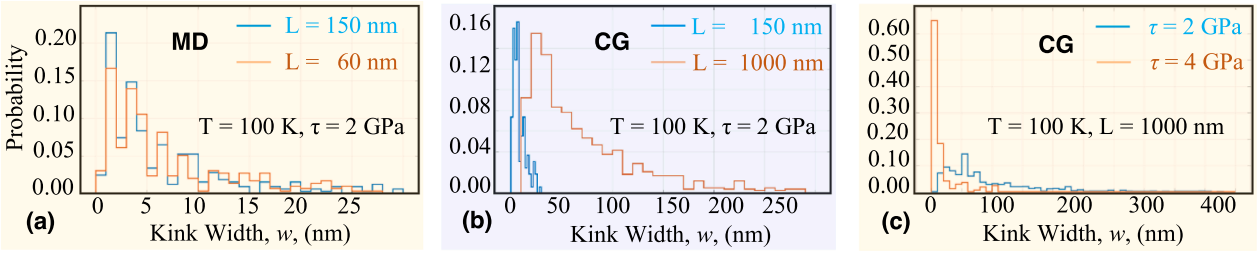

Fig. 3. A characterization of the dislocation line length and stress dependence of the kink width distribution from full MD and also CG simulations: (a-b) results from MD and CG simulations of the kink dynamics on a dislocation line with different lengths at $T = 100$ K and $\tau = 2$ GPa; (c) results from CG simulations for $L = 1000$ nm at $T = 100$ K when the applied shear stress increases from $\tau = 2$ GPa to $\tau = 4$ GPa.

between $\mathbf{f}^T(\boldsymbol{x},t)$and $-\beta\nabla T(\mathbf{x},t)+\boldsymbol{\eta}(t)$such that the linear momentum equation, i.e., Eq. (3), reproduces results that satisfy the kinetic energy-temperature relation for a system at thermal equilibrium. A detailed mathematical derivation can be found in [105], which shows that the random force $\boldsymbol{\eta}(t)$ must be accompanied by a friction (or damping) force for a system to reach thermal equilibrium at long times and that$\mathbf{f}^D(\boldsymbol{x},t)$ has the form of a viscous force. In [105], two forms of$\mathbf{f}^D(\boldsymbol{x},t)$ were introduced: (i) a delta-correlated white noise, and (ii) a time correlated Gaussian process, the latter of which can be expressed as

$$\begin{aligned}&\mathbf{f}^D(\boldsymbol{x},t)=\int_0^t\gamma(t-\tau)\mathbf{v}_\alpha d\tau \text{ for } \langle\eta_i(t)\eta_j(\tau)\rangle=C(t-\tau)\delta_{ij}\\&\text{where } C(t-\tau)=\frac{2g}{e\sqrt{2\pi}}\exp\left[-\frac{(t-\tau)^2}{2e^2}\right]=k_BT\gamma(t-\tau)\end{aligned}\tag{7}$$

where e is the standard deviation and 2g is the strength of $\boldsymbol{\eta}$(t). The widely studied trigonometric representation for Gaussian processes can be used to generate the fluctuation force caused by the short-wavelength phonons omitted by the FE tri-linear shape functions, i.e.,

$$\eta_i(t)=\sum_{n=0}^{N_c-1}[A_n\cos(\omega_nt)+B_n\cos(\omega_nt)],\tag{8}$$

where N_c is the total number of omitted phonons in each element, ω_n are the frequencies of the omitted phonons, and A_n and B_n are mutually independent Gaussian random variables. The parameters, N_c and ω_n, can be found from the phonon dispersion relations [105] or the phonon density of states (PDoS); A_n and B_n are mutually independent Gaussian random variables having zero mean and variance C (0) such that

$$<A_nB_m>=0 and <A_nA_m>=<B_nB_m>=C(0)\delta_{nm}.\tag{9}$$

Although the full MD simulation has been performed here to pre-calculate the PDoS for determining the parameters in Eq. (8), it does not defeat the FT-CG yet because the simulation cell size in MD is at nanometer scale, which is orders of magnitudes of smaller than that in FT-CG when the motion of a μm-long dislocation is concerned.

Approximating the displacement field within each FE as $\mathbf{u}(\mathbf{x})=\Phi_\eta(\mathbf{x})U_\eta$, the weak form of Eq. (3) can be written as

$$\begin{aligned}&\left(\int\int\int_{V_e}\rho\Phi_\xi\Phi_\eta dV\right)\ddot{U}_{\eta\alpha}+\left(\int\int\int_{V_e}\rho\Phi_\xi\Phi_\eta\int_{t-t_c}^{t}\gamma(t-\tau)\dot{U}_{\eta\alpha}(\tau)d\tau dV\right)\\&=\int\int\int_{V_e}\Phi_\xi\mathbf{f}^{\text{int}}dV-\int\int\int_{V_e}\Phi_\xi(\beta\nabla T+\boldsymbol{\eta}(t))dV,\end{aligned}\tag{10}$$

where $\Phi_\xi(\mathbf{x})$ and $\Phi_\eta(\mathbf{x})$ are shape functions; $U_{\eta\alpha}$, $\dot{U}_{\eta\alpha}$, and $\ddot{U}_{\eta\alpha}$ are the displacements, velocity, and acceleration of the α-th atom within the η-th FE node. The integrals in Eq. (10) can be evaluated using Gaussian quadrature. For the FEs employing the tri-linear shape functions, the temperature gradient in the last term is either zero for a thermal equilibrium or a constant for steady state. In either case, no numerical integration is needed for the last integral, as $\nabla T+\boldsymbol{\eta}(t)$ does not vary in space within a finite element.

3. Simulation results

In this section, we first benchmark the predictive capability of the FT-CG method by characterizing: **(a)** the effects of a pre-existing dislocation on the PDoS of bcc W at finite temperature; and **(b)** the stress-and temperature-dependence of a dislocation core structure. Thereafter, we report the atomistic-to-microscale FT-CG simulation results on the temperature-, stress-, and line length-dependence of kink activation volume and enthalpy. For validation, these results are also compared with those from DFT, full MD simulations, and also experimental results whenever possible.

3.1. *Dislocation-induced PDoS degeneration at t = 300 K*

The PDoS of a perfect single crystal at a given temperature is deterministic. Here, we first perform nanoscale MD simulations of the dynamic relaxation of a bcc W sample containing 1024,000 atoms for 200 ps under zero stress at $T=300$ K. The atomic velocity correlation and its Fourier transformation are then calculated. The green curve in Fig. 4a presents the MD-simulation-based PDoS, noted as $g(\omega)$, for single crystal bcc W at $T=300$ K. The PDoS of a bcc crystal has two typical signatures: **(a)** near the long-wavelength/low-frequency limit ($\omega<2$ THz in Fig. 4a), no well-pronounced peaks appear, and $g(\omega)$ can be approximately considered as a function of ω^2; **(b)** in the short-wavelength/high-frequency domain ($\omega>2$ THz in Fig. 4a), three main peaks appear in $g(\omega)$, which are induced by two transverse phonon modes and one longitudinal phonon mode, respectively. This is consistent with the experimental observations from the nuclear resonant inelastic scattering of synchrotron radiation [82].

The three peaks in the PDoS (green curve in Fig. 4a) predicted from full MD cannot be all captured using our existing CG models [57–63]. The reason is that the FE procedure in those CG models cuts off the phonons with wavelengths shorter than λ_c or frequencies higher than ω_c. In particular, if the FE with an edge length of l is used for the sample discretization, phonons with wavelengths less than $\lambda_c=4l$ will be cut off [83,84]. When a characterization of the thermally-induced kink dynamics on a dislocation line becomes desired, the high-frequency/short-wavelength phonons with ($\omega_i>\omega_c$ and $\lambda_i<\lambda_c$) must be included in the CG scheme because these short-wavelength phonons considerably affect the atomic-level kink activities and the dislocation mobility. One approach of including these high-frequency phonons is using a lattice-dynamics (LD)-based shape function with short-wavelength enrichment to supplement with the linear element shape functions [83]. Despite its success in enabling the passage of a short-wavelength phonon from the atomistic to the CG region, such approaches are, however, difficult to implement here because the development of an LD-based shape function for the crystal containing a dislocation is non-trivial where the periodic symmetry has been broken. As such, instead of explicitly including the short-wavelength phonon modes through shape function enrichment, here we: **(1)** choose ω_i in Eq. (8) to be ω_1, ω_2, ω_3, …, and ω_n according to the MD simulation-predicted PDoS for bcc W as shown in Fig. 4a; **(2)** substitute Eq. (8) into Eq. (5) and Eq. (7) to calculate the temperature-induced forces $\boldsymbol{f}^T(\boldsymbol{x},t)$; **(3)** perform the time integration of Eq. (10); **(4)** generate the PDoS from such FT-CG simulations by computing the autocorrelation of the FE nodal velocities; **(5)** quantify the difference between the obtained PDoS and that from full MD; (6) repeat Step-1 to Step-5 by iteratively tuning the value of A_i and B_i in Eq. (8) until a minimum difference between the FT-CG- and MD-based PDoS is achieved. In this way, a set of optimized values for ω_i, A_i, and B_i are determined. The resulting FT-CG model can reasonably include the contribution of short-wavelength phonons to the overall crystal dynamics, especially if we choose the frequencies, ω_i, according to a full MD-based PDoS. This is validated by achieving a good agreement between the red and the green curves in Fig. 4a, which shows that the PDoS from such a FT-CG (2000 FEs, 512 atoms per FE) model agrees well with the full MD-based PDoS. The three peaks, which were absent in our previous CG simulations using the tri-linear FE shape functions, are captured here. This is, however, not surprising since the frequencies around those peaks have been enforced through a deployment of Eq. (8) using the chosen ω_1, ω_2, and ω_3.

To demonstrate the predictive capability of such an FT-CG model, we introduce a screw dislocation line into the FT-CG model, but do not change the values of ω_i, A_i, and B_i that we have already identified. The FT-CG model containing a pre-existing dislocation is then relaxed for 200 ps at $T=300$ K. Fig. 4b presents the FT-CG-predicted PDoS of a local domain around the dislocation and its comparison with MD simulation

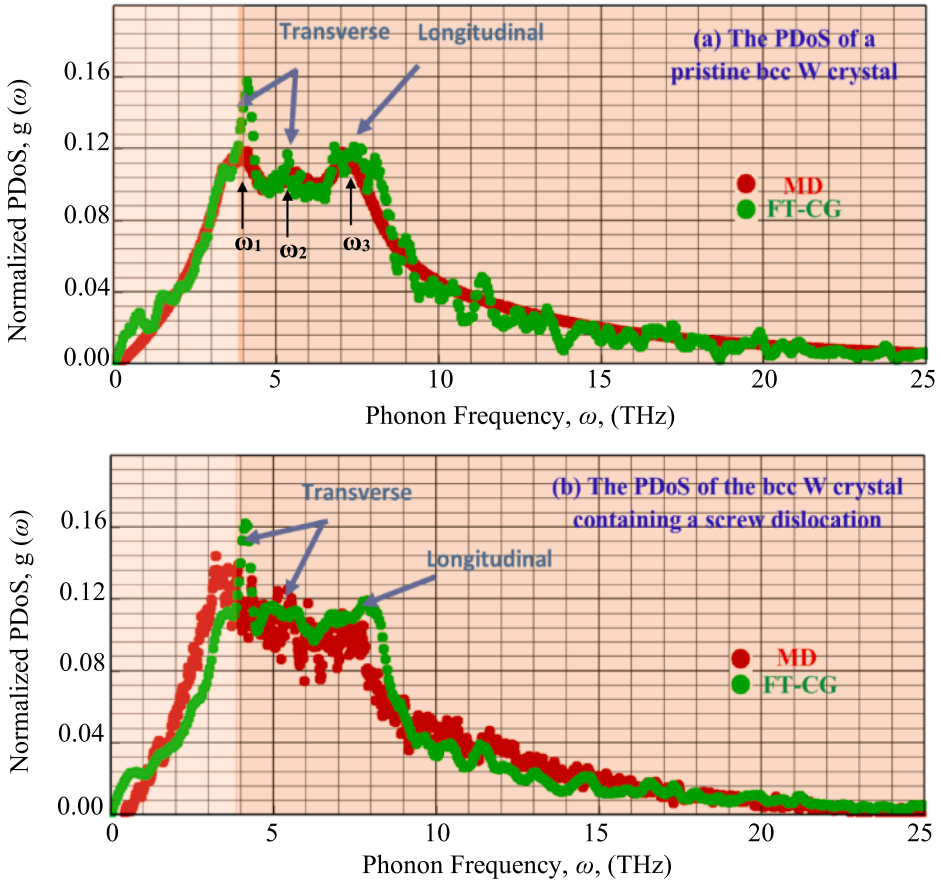

Fig. 4. The normalized PDoS, $g(\omega)$, extracted from FT-CG simulations (red, 512 atoms per FE) and its comparison with that from full MD simulations (green): (a) the PDoS of a pristine single crystalline W at $T = 300$ K; (b) the FT-CG (red, 512 atoms per FE) and MD-simulation-predicted PDoS degeneration induced by a screw dislocation in bcc W at $T = 300$ K.

results. Consistent with MD, the FT-CG recovers the dislocation-induced changes in the PDoS: **(i)** comparing with the sharp peaks in the PDoS of a pristine crystal (Fig. 4a), the peaks in the PDoS for a defected sample (Fig. 4b) are seen to broaden due to the occurrence of the dislocation-phonon scattering; **(ii)** after the dislocation is introduced, additional peaks (also referred as defect modes) appear in the PDoS as a result of the localized vibration and its interaction with the local stress/strain around the dislocation; **(iii)** in the presence of the screw dislocation, the height of the longitudinal peak significantly decreases. Such a decrease implies: **(a)** the screw dislocation line vibrates at longer wavelengths and lower frequencies; **(b)** the screw dislocation prefers low-frequency, long-wavelength solutions. Such solutions will promote the formation of string cusps, i.e., kinks, to assist their motion through a steep, corrugated energy landscape. Obviously, the FT-CG provides us with a reliable estimate on the effects of the dislocation on the PDoS. It goes beyond the traditional continuum theories that do not resolve or at most have only limited resolution near a core, where defect-induced vibration modes are manifested and can not be simply ignored.

3.2. *Non-degenerate core structure under zero stress at 0 K*

To demonstrate the capability of the FT-CG model in retaining the atomistic nature of dislocation dynamics, we first present results to show that it can resolve the atomic-level core structure (non-planar, compact) of a screw dislocation line in bcc W under zero stress at 0 K. Fig. 5 shows the core structure of a screw dislocation in bcc W from a CG simulation using Proville-EAM potential [76] and its comparison with that from molecular statics (MS) simulations. Here the sample has a dimension of 100 nm × 250 nm × 200 nm along *x*, *y*, and *z* directions, respectively. It is discretized into 157,320 rhombohedral-shaped FEs (1728 atoms per FE) away from the dislocation core together with 2160 triangular-prism-shaped FEs (864 atoms per FE) nearby the core. This model corresponds to ~274 million atoms in a full MS model. A ½[111] screw dislocation is introduced at the center of the simulation cell by applying the elastic solution of the displacement field of a dislocation to the FE nodes. The nodal positions are then relaxed with a PBC along all three directions. Thereafter, the CG model containing the dislocation is relaxed for 20 ps with a viscous damping of 0.01. An analysis of the time evolution of the potential energy confirms that an equilibrium state of the CG system has been achieved through such a dynamic relaxation. This equilibrium state is believed to be comparable with that from MS simulations at 0 K.

The core structure of the dislocation in the CG model is then characterized via the displacement differential map analysis [85,86] through several steps: **(1)** extract the positions of the atoms embedded within the coarse FEs as an interpolation of the nodal positions of the FEs with their configuration (Fig. 5a) being relaxed from CG simulations; **(2)** identify the atoms which participate in the dislocation core through a first-neighbor coordination number analysis around one segment of the dislocation line. This segment is located in the middle of the sample. The length of this segment is 2*b* (*b* is the Burgers vector); **(3)** calculate the atomistic differential displacement following the strategy in [86] and create the differential displacement maps (Fig. 5b) for a quantitative description of the core structure. In Fig. 5b, the purple solid lines are the boundaries of FEs in CG and the red particles are the atoms, whose locations are determined through an interpolation of FE nodal positions. Here the dislocation core is schematically presented by three black arrows connecting the three atomic rows forming a triangular prism. The

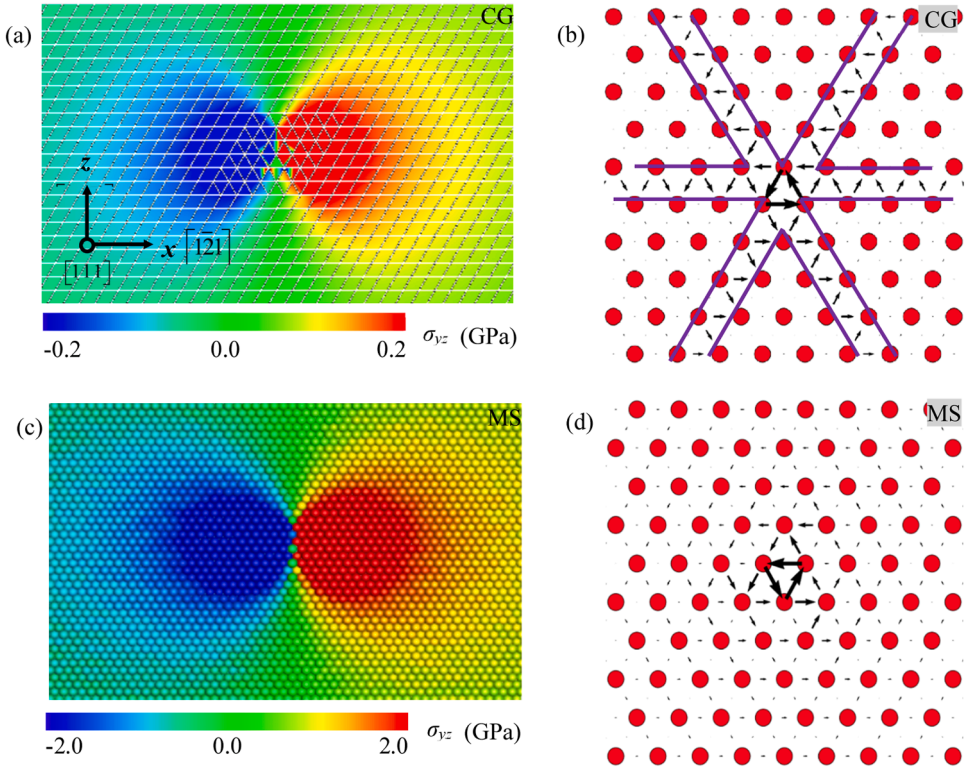

Fig. 5. The CG-simulation-predicted core structure of a screw dislocation in bcc W under zero stress at 0 K and comparison with that from MS calculations: (a) the FE configuration and stress contour near the core in CG (1728 atoms per FE away from the core and 864 atoms per FE nearby the core); (b) the CG-simulation-extracted atomic arrangement and atomistic displacement differential map near the dislocation core (purple lines show the FE boundaries); and (c, d) the relevant results from MS simulations.

atoms in those three rows are positioned on a helix, which wind up in a counterclockwise manner. The lengths of those arrows, i.e., the magnitudes of the atomistic differential displacement, are normalized by $b/3$ and represent the atomic displacement with respect to the pristine bcc atomic positions along the [111] direction. For validation, results from full MS simulations are also plotted (Fig. 5c, d). Our major findings here are: **(a)** the CG model successfully produces the compact, non-degenerate dislocation core structure, which is fully comparable to that from DFT/MS calculations [5,86], although only at a fraction of their cost; **(b)** the nonlocal nature of the CG model enables it to predict a finite stress at a level of ~2 GPa very close to the dislocation core (Fig. 5a,c), which will be infinite if one follows the classical theory of linear elasticity [40]. Such a local stress state may modify the Peierls barrier on the three possible glide planes of the screw dislocation and thereby change the kink-pair activation energy barrier or activation volume on these planes; **(c)** the CG simulation-predicted core structure (Fig. 5b, d) is invariant with respect to the [101] dyad and spreads symmetrically onto three {110} planes. This is the same as that in DFT/MS calculations [5,85,86]. As such, the applicability of a Proville-EAM-based CG model is benchmarked through explicitly describing the atomic-level core structure of a dislocation in bcc metals at a fraction of the cost of DFT/MS calculations.

3.3. *Dislocation core structure under non-zero stress at finite temperature*

When the bcc W sample containing an initially built-in dislocation line is subjected to a shear stress (noted as τ_{ap}, shearing along the dislocation line direction, see details on how the shear is applied in Fig. 1a) at finite temperature, kinks may be activated. Kink activation will cause a change of the core structure. Fig. 6a and 6b present the snapshots of the time sequence of the atomic-level core structure evolution along the dislocation line observed in FT-CG (512 atoms per FE) and MD simulations using the Proville-EAM potential [76]. It is seen that: **(a)** under $\tau_{ap} = 1.6$ GPa at $T = 1000$ K, the dislocation line starts to become rough due to the kink activations; **(b)** upon multi-kink formation on the dislocation line, a co-existence of the kinked (red), non-kinked (blue), as well as the intermediate (green) core segment is observed in both FT-CG and MD simulations, although the results from FT-CG are not exactly the same as that in MD due to the stochastic time-dependent nature of the multi-kink formation; **(c)** the activated kinks migrate along the dislocation line, transform its core structure from a "soft" configuration (compact core, lower energy), to an intermediate configuration (green), and then to a "hard" configuration (a split core, higher energy, unstable under finite stress and temperature); **(d)** the core structure transformation from "compact, non-degenerate" to "split, degenerate" enables the admission of kinks with a height of $\sqrt{2}b/6$, which are referred as half-height kinks; **(e)** due to the metastability of such a split core, after the nucleation of a one half-height kink pair, another half-height kink pair in the same direction will be also activated nearby, migrate along the dislocation line, annihilate with its neighbors, and then advance the dislocation segment forward by one lattice spacing with its core structure back to compact again (Fig. 6a, b).

It should be emphasized that the Proville-EAM potential [76] used in FT-CG and MD simulation has been shown to be capable in predicting a compact non-degenerate core for a screw dislocation under zero stress at 0 K, in agreement with *ab initio* calculations. Therefore, the extended split core structure in Fig. 6a, b is believed to be caused only by the uncorrelated kink pair formation activated by the non-zero stress at finite temperature. It is not from the common artifacts of many other interatomic atomic potentials, such as the one by Ackland and Thetford (noted as the AT-EAM), for bcc metals [88]. The AT-EAM potential predicts a Peierls potential barrier with two maxima separated by a pronounced minimum at the halfway position. This is usually referred as double-hump potential and differs from *ab initio* calculations that give

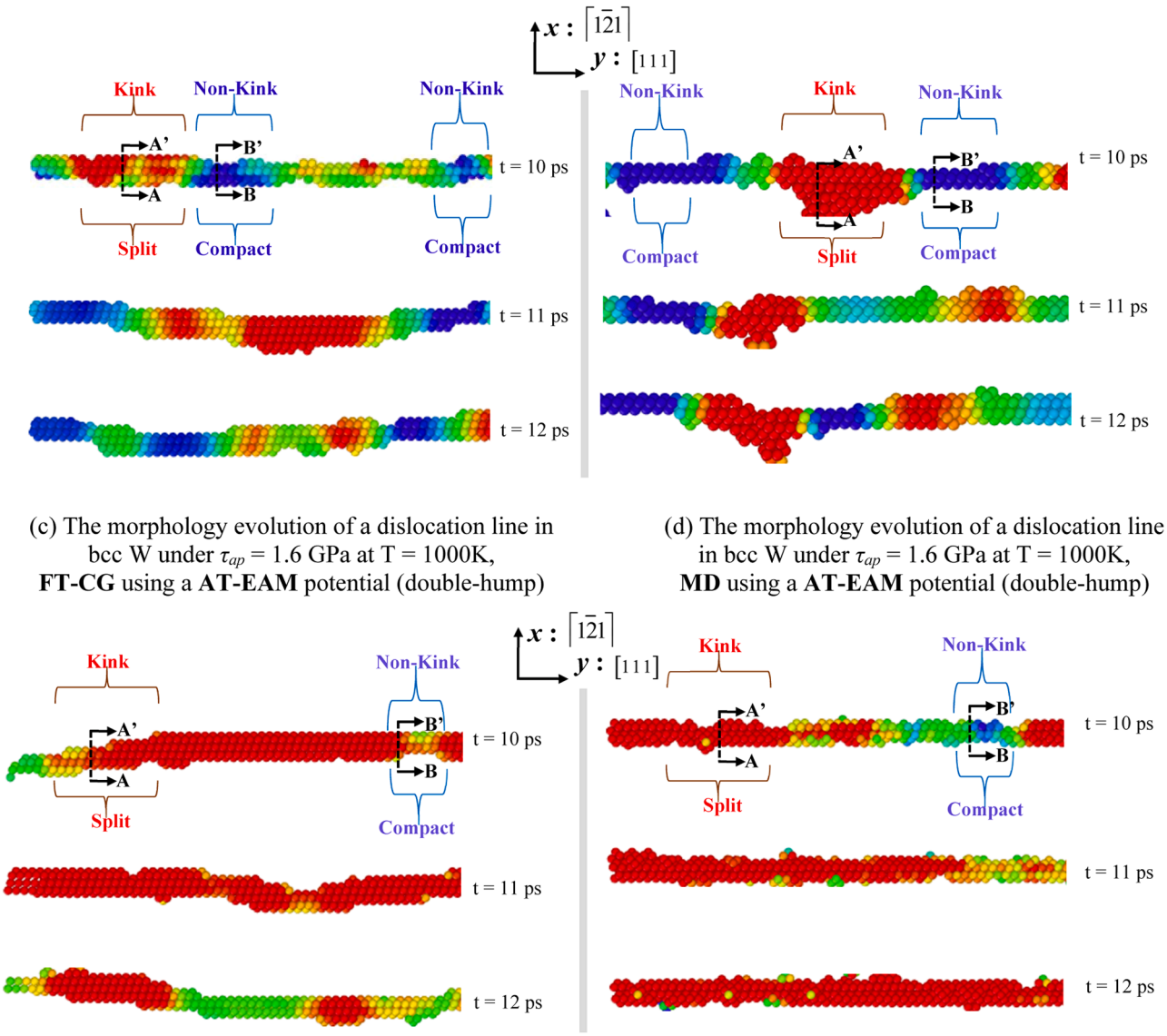

Fig. 6. The atomistic core structures along a kinked dislocation line with a length of 44 nm in bcc W by FT-CG (512 atoms per FE) and MD using (a, b) the Proville-EAM and (c, d) the AT-EAM potential, respectively. Only the atoms that participate in the cores are displayed and colored according to the coordination number using OVITO [87].

rise to only one maximum. Such double-humped potentials usually lead to a degeneration/splitting of the core structure at the saddle point even under zero stress at 0 K. When the dislocation line with an initially degenerated core structure is subjected to a stress at finite temperature, the mechanism underlying the motion of it can largely differ from that starting with a compact dislocation core. As evidence of it, Fig. 6c and 6d show the atomic-scale core structure evolution along a dislocation line in bcc W by FT-CG and MD simulations using AT-EAM potentials, respectively. Comparing with results in Fig. 6a, b, several major observations in Fig. 6c, d are: (1) the core structure of the entire dislocation line splits, and there is no compact core along the dislocation; (2) the core splitting caused by kink formation can not be differentiated from the splitting caused by the artifacts of the AT-EAM potential. Consequently, such double-humped potential may promote kink nucleation, easier the dislocation motion, lower the flow stress, and amplify the line length dependence of the kink activation energy/volume. This will be quantitatively analyzed in more detail in a later section of this paper.

3.4. The kink-induced core structure degeneration under non-zero stress at finite temperature

To benchmark the capability of FT-CG in predicting the kink-induced core structure transition from "compact" to "split", Fig. 7a–d present the instantaneous snapshots of FE configuration, atomistic displacement differential map, and local stresses on the AA' and BB' cross-sections (Fig. 6a, b) of a dislocation line obtained from Proville-EAM potential-based FT-CG and MD simulations, respectively. Different from the steady stress field (Fig. 5a) around the non-moving, compact core under zero stress, the stresses near the moving dislocation core under $\tau_{ap} = 1.6$ GPa and $T = 1000$ K exhibit a strong thermally-induced fluctuation. It is seen that the stochastic nature of such a thermally-induced stress fluctuation has been reasonably retained using FT-CG (Fig. 7a), albeit at a

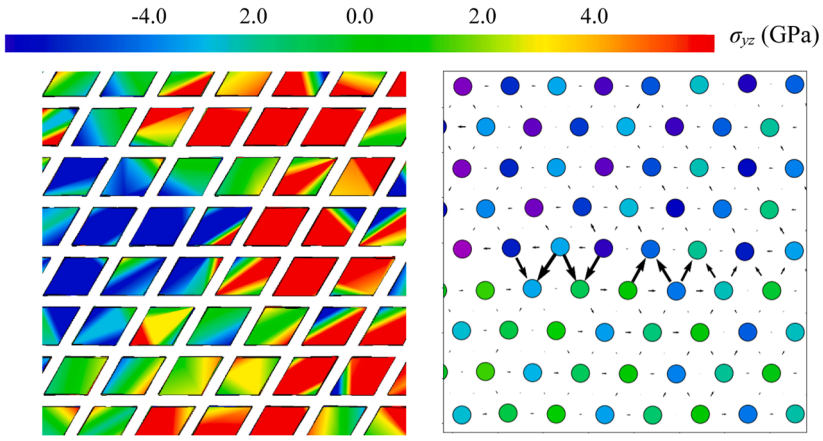

(a) Stresses and core structures of a kinked dislocation (AA' in Fig. 6a) by FT-CG (512 atoms per FE).

(b) Stresses and core structures of a non-kinked dislocation (BB' in Fig. 6a) by FT-CG (512 atoms per FE).

Fig. 7. The local stress and the structure of a split dislocation core in bcc W under shear (τ_{ap} = 1.6 GPa) at a finite temperature of T = 1000K: (a-b) FE mesh deformation, local stress contours, and atomistic displacement differential map of a kinked (AA' cross-section in Fig. 6a) and non-kinked dislocation (BB' cross-section in Fig. 6a) extracted from the Proville-EAM-based FT-CG simulations; (c, d) the atomic-level local stress contour together with the atomistic displacement differential map around the core of a kinked (AA' cross-section in Fig. 6b) and non-kinked (BB' cross-section in Fig. 6b) from full MD simulations.

lower resolution than that in MD (Fig. 7c) due to the use of a CG description. More importantly, comparing with the planar structure of the core under no stress and 0 K (Fig. 5), an atomistic displacement differential map analysis of the results from both FT-CG and MD (Fig. 7a and c) clearly shows that the dislocation core has transformed into a planar structure due to the kink activation. Such a split/planar core structure transforms back to compact (Fig. 7b, c) when kink-pairs annihilate with each other, which in turn, results in the advancement of the segment by one lattice spacing. Such observations are believed to be reasonable because: **(i)** the DFT-predicted non-planar, compact core structure is for a dislocation in an infinite medium under zero stress at 0 K, which is obviously not the case in Figs. 6 and 7. For a dislocation line within a finite-sized sample exposed to a non-zero stress at finite temperature, the kink-pair forms and the compact core splits; **(ii)** the core structure of the screw dislocation in bcc crystals is influenced not only by the shear stress that drives the dislocation motion in the slip plane, but also by other stress components, such as the stress normal to the slip plane. A confinement of the sample on its boundaries produces a non-negligible normal stress, which constricts the core along a direction normal to the slip plane and expands its width in the slip plane; **(iii)** according to Hirsch and Sun [89], the anisotropic elasticity favors the split core structures for a screw dislocation in bcc metals under non-zero stress. Such anisotropy is present and retained in both FT-CG and MD simulations.

3.5. *Temperature- and Dislocation line length-dependence of the flow stress*

At a fundamental level, we believe the kink-induced core structure transition contributes to the temperature (noted as T) and the dislocation line length (noted as L) dependence of the flow stress because: **(i)** both the kink structures (widths, heights, core configuration) and kink dynamics (activation volume, activation enthalpy, diffusion coefficient, mean free path) are all sensitive to T and L [8–15,23,33–36,41]; **(ii)** such complex kink dynamics dictates the mobility of a screw dislocation in bcc W when subjected to a shear at finite temperature; and **(iii)** the mobility of each individual screw dislocation, in principle, determines the overall flow stress of materials.

As an attempt of quantifying the temperature- and the line length-dependences, Fig. 8a presents the flow stresses, noted as σ_f, predicted from FT-CG simulations of the motion of a single screw dislocation line in a bcc W sample under shear at different temperatures. Dislocation lines with lengths ranging from 60 nm to 1 μm are considered. The experimentally measured flow stresses of single crystalline W under deformation at different temperatures [90,91] are also provided here for comparison. In these experiments, the orientation of the tensile specimen with an initial dislocation density of $10^{10}/m^2$ was characterized by two angles noted as $\kappa_0 = 40^\circ$ and $\lambda_0 = 50^\circ$, where κ_0 is the angle between the primary slip plane (110) and the crystal tensile axis. λ_0 is the angle between the crystal tensile axis and the primary slip direction [111]. The resolved shear stress was then calculated by means of the Schmid factor for (110) [111] slip and used to compare with σ_f obtained in this work.

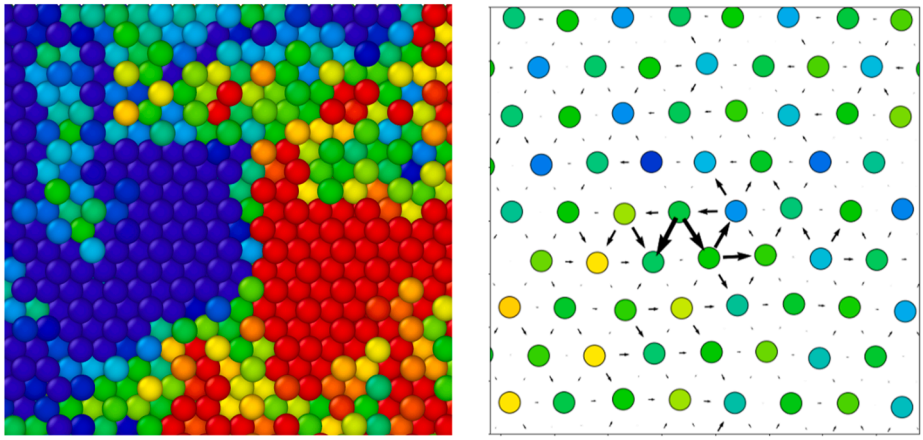

(c) Stresses and core structures of a kinked dislocation (AA' in Fig. 6b) by MD.

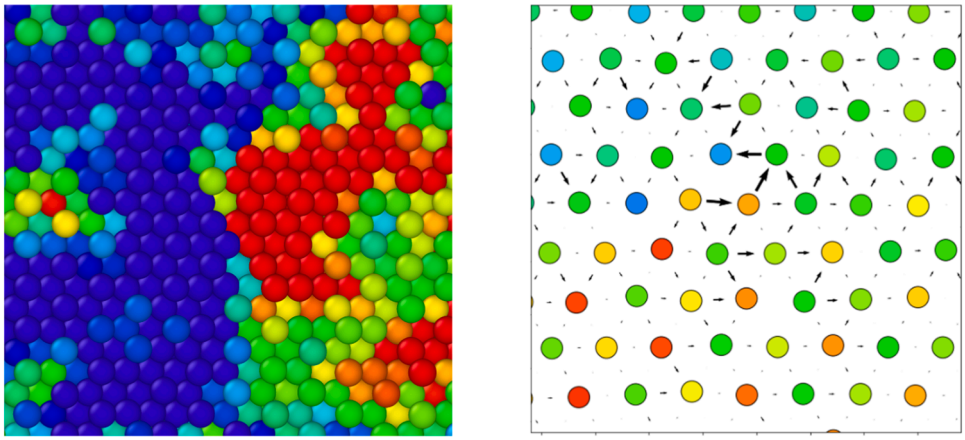

(d) Stresses and core structures of a non-kinked dislocation (BB' in Fig. 6b) by MD.

Fig. 7. (*continued*).

In Fig. 8a, σ_f is taken as the stress at which a kink-pair starts to appear on a dislocation. Each FT-CG simulation starts with a fully relaxed structure. A constant temperature, T, is then imposed with the applied shear being increased incrementally. Thereafter each stress increment, a finite-duration equilibration has been followed for the system to respond at this new stress level. Thus, the results in Fig. 8 are not from high-strain rate deformation. Instead, each data point in Fig. 8 is from one FT-CG simulation under constant shear-stress loading. With that, we would like to argue that our results in Sections A, B, C, D, E, and F derived from the data in Fig. 8 are all from quasi-static simulations, which thus have no short timescale or high strain-rate issues. Also, the data in Fig. 8 are all normalized by σ_0. Here σ_0 is the critical stress required for activating the kink on the dislocation line at $T = 0$ K. It pertains only to kink nucleation and is well below the Peierls stress for activating the motion of the dislocation line. Our FT-CG simulations show that the values of σ_0 for dislocation lines with different lengths differ: the longer the dislocation line, the lower the σ_0. In particular, $\sigma_0 = 2.12$ GPa for $L = 60$ nm and $\sigma_0 = 1.96$ GPa for $L = 1000$ nm. By contrast, the experimental results [90,91] in Fig. 8a are normalized by a much lower Peierls stress $\sigma_0 = 0.6$ GPa. The reasons why the interatomic potential-based simulations always predict a higher σ_0 than that in experiments has been extensively discussed elsewhere [6,92].

Several major findings emerge from Fig. 8a: **(a)** for all the different dislocation line lengths under consideration, the FT-CG simulations using both the Proville- and the AT-EAM potential predict a decrease of σ_f upon the increase of temperature; **(b)** σ_f exhibits a non-uniform dependence on temperature, T. In detail, σ_f decreases significantly faster when $T < T_k$ than it does when $T > T_k$ (Fig. 8a). This is qualitatively consistent with experimental data [90,91]. When $T > T_k$, the thermal energy may contribute more to kink-pair formation, dislocation migration, and plastic flow by reducing the stress required for dislocation motion; **(c)** when the dislocation line is exposed to the same temperature, the double-humped AT-EAM potential predicts a significantly lower flow stress than the single-humped Proville-EAM potential because the core structure degeneration and kink-pair formation have been artificially promoted in the AT-EAM simulation; **(d)** quantitatively, the σ_f - T relation extracted from FT-CG simulations using both Proville- and AT-EAM potentials approach the experimental results when the dislocation line length increases from 60 nm to 1 μm. We speculate that the σ_f - T relation that could be extracted from FT-CG simulations of the motion of longer dislocation lines (>1 μm) will possibly be in even better agreement with the experimental data.

However, it should be also noted that a one-to-one correspondence between the computational and experimental results of the σ_f - T relation will not be achieved by simply increasing L alone here, for several reasons. First, here we have only considered the motion of a single dislocation line. The interaction between this dislocation and its neighbors in the plastically deformed sample is not yet explicitly incorporated into the present model. By contrast, the flow stress measured from the experiments in [90,91] is for the collective behavior of a group of dislocation lines, although the dislocation density in experiments is as low as $10^{10}/m^2$. Second, the flow stress of materials usually exhibits a non-negligible sensitivity to solid-solution contents, vacancies, interstitials, and many other defects, which are all present in experiments

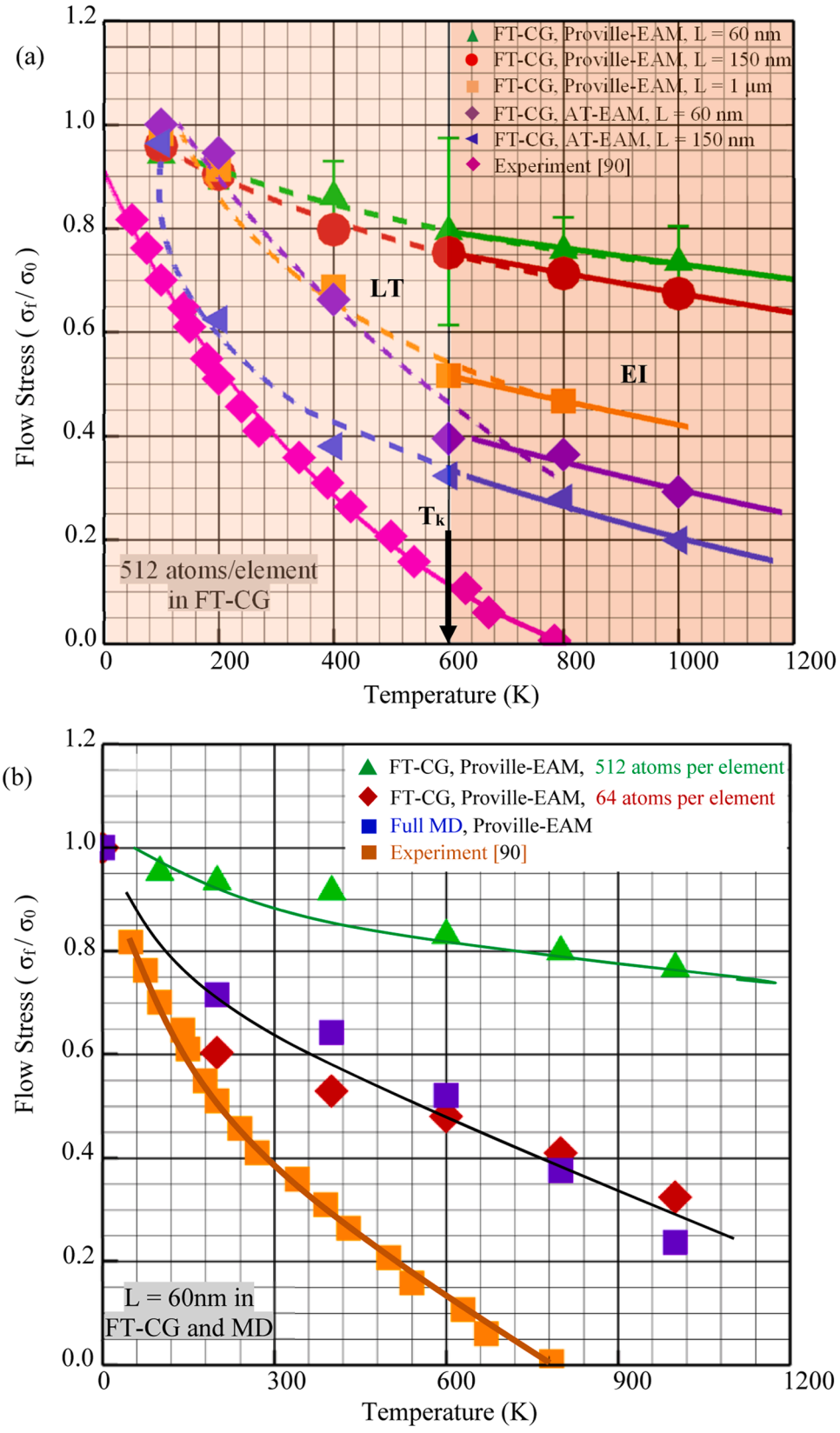

Fig. 8. The temperature dependence of the normalized flow stress (σ_f, normalized by the critical stress, σ_0) in bcc W characterized from FT-CG simulations and its comparison with that from MD and experiments: (a) the dislocation line length increases from 60 nm to 1 μm in FT-CG with 512 atoms per FE; (b) the coarse FEs in the FT-CG models are refined to 64 atoms per FE and then to fully atomistic resolution, i.e., MD.

[90,91] but not yet included into the present FT-CG simulations. They can be incorporated if desired [93]. Third, according to the extensive discussion in the literature [6,92], the EAM potential used here has overestimated (generally around 2–3 times the experimentally measured value) the Peierls stress of ½[111] screw dislocations in bcc crystals. If an experimentally comparable flow stress is desired, an incorporation of the quantum effect [6] into the simulations, e.g., through the deployment of the interatomic potential trained from the DFT data using machine learning algorithm [86,94], may become necessary. Fourth, the flow stress from our FT-CG simulation is measured when kink-pairs start to nucleate, which is believed to provide only an upper bound of the true flow stress. Fifth, the actual stress acting on an individual dislocation line can be indeed a few times larger than the flow stress measured in experiments since the dislocation line in the plastically deformed sample can be embedded within a high local stress field induced by dislocation interactions, pileups, mobile edge dislocations, or interstitial impurities. Instead, the actual local critical stress required for moving one single dislocation line has been accurately measured in the present simulations. The flow stress may have been largely underestimated in experiments because only a critical value of the overall applied stress is considered, rather than the local stress on one isolated dislocation. Finally, the scatter of the flow stress data in both FT-CG simulations (see the error bar in Fig. 8a for $L = 60$ nm) and experiments is unavoidable. For instance, the flow stresses measured from our FT-CG simulations are found to be highly sensitive to the size of the FE meshes. When the FE meshes are refined from 512 atoms per FE to 64 atoms per FE and then to the fully atomistic level, the FT-CG simulation-predicted flow stress decreases and moves closer to experimental results (Fig. 8b). Comparing with the 64-atom FE, the FT-CG simulation using the 512-atom FE does overestimate the flow stress, especially when the temperature is above 300 K. We attribute it to two reasons: **(i)** here we include the short-wavelength and high-frequency phonons into the current FT-CG through Eq. (8), in which the parameters (A, B, and ω) are calibrated at 300 K. Rigorously speaking, if one desires an accurate prediction from FT-CG above 300 K, the calibration of Eq. (8) needs to be calibrated in the high temperature regimes to include a larger population of short-wave length/high-frequency phonons; **(ii)** a deployment of the tri-linear FE shape function in FT-CG leads to an overestimation of the kink-width (see Figs. 2, 3), and then a higher stress (Fig. 8b) for activating a kink. Computationally, the FT-CG using 512 atoms per FE is significantly more efficient than that using 64 atoms per FE. So we choose the 512-atom FEs for FT-CG simulations of μm-long dislocations. A reliable assessment of the temperature dependence of the flow stress at an optimum tradeoff between efficiency and accuracy in computations demands a careful design of simulation conditions. Addressing all these sources of simulation-experiment mismatch is non-trivial and warrant more comprehensive research.

3.6. Calibrating the line tension (LT) and elastic interaction (EI) models

Despite these caveats, Fig. 8 still indicates that the sensitivity of the flow stress to temperature has been qualitatively captured by FT-CG simulations. This is a key aspect of dislocation behavior in bcc crystals at finite temperature. Although not yet matching experimental data in view of various factors articulated in the previous section, the results in Fig. 8 reinforce the use of FT-CG models for a given interatomic potential to characterize the thermally activated kink dynamics, such as kink activation enthalpy (ΔH) and activation volume (ΔV), on a dislocation line with its lengths spanning from nanometers to micrometers through "temperature jump tests" and "strain rate jump tests", respectively. In such tests, the $\Delta\sigma_f$ - ΔT relation, i.e., the change of the flow stress upon a change of the temperature, rather than the $\sigma_f - T$ relation, determines ΔH and ΔV. Different from the $\sigma_f - T$ relation, the FT-CG simulation-based correlation between $\Delta\sigma_f$ and ΔT has a potential to reasonably represent the experimental result. Moreover, the use of FT-CG models facilitates us to calibrate the LT model for understanding the kink-controlled dislocation dynamics in continuum models by informing them with model parameters and mechanism-based constitutive rules to describe the plastic flow in bcc transition metals at the mesoscale.

Here we demonstrate how the FT-CG simulation results can be utilized to calibrate continuum models, e.g., the EI model by Seeger [12,13] and the LT model by Dorn and Rajnak [11]. Taking the result in Fig. 8a for W as an example, the FT-CG simulation-predicted $\sigma_f - T$ relation is divided into two regimes: **(i)** in Regime-I, $T < T_k$ with $T_k =$ 600 K, the flow stress decreases with the increase of the temperature in a parabolic manner approximately. At $T \approx T_k$, the parabolic σ_f–T relation terminates and marks the onset of a non-uniform temperature dependence of σ_f; **(ii)** in Regime-II, $T > T_k$, the flow stress decreases linearly with the increasing temperature. In this regime, the variation of the flow stress upon the change of the temperature is remarkably smaller than that in Regime-I. There obviously exists a rather abrupt transition between Regime-I and Regime-II. According to Seeger [12,13], such a transition from "the linear Regime-II" to "the parabolic Regime-I" is noted as "the upper bend", with T_k being noted as "the knee temperature". The sharp rise of σ_f at a low temperature is considered as one most important features of plastic deformation behavior of bcc crystals, and is also recognized as a primary causal factor in the ductile-to-brittle transition (DBT) in these materials. In Fig. 8a, the stress required to enter from Regime-II to Regime-I is found to decrease from $0.85\sigma_f / \sigma_0$ to 0.50 σ_f / σ_0 when the dislocation line length increases from 60 nm to 1 μm. This finding suggests that the critical stress for DBT in bcc metals is sensitive to the average lengths of mobile dislocation lines within them.

To interpret the above observations from a theoretical point of view, the LT and EI models derived from the kink-pair theory are used here. In this theory, the motion of the screw dislocations is considered to be mediated by thermally activated kink-pair formation and migration along the dislocation line. According to this theory, when the stress level is low but the temperature is high (the EI regime in Fig. 8a), the dislocation dynamics is determined by the elastic interaction between kinks in terms of $1/r$, where r is the distance between two kinks on the dislocation line. In this regime, multiple kink pairs are simultaneously activated on a dislocation line and a temperature dependence of the flow stress associated with the motion of the dislocation line can be approximated by Eq. (11) [95]. By contrast, when the bcc crystal is deformed at low temperature (the LT regime in Fig. 8a), the density of kinks is much lower and the average spacing between those kinks is larger than that in the EI regime. Under such conditions, kink-kink interactions contribute less than kink nucleation to the dislocation dynamics. Correspondingly, the temperature dependence of the flow stress in this regime is approximated by Eq. (12) according to the LT model [95]. When combining Eq. (11) and Eq. (12) into one diagram, a hump appears and marks the transition between the EI and LT regimes.

$$\sigma_f^{1/2} = A_{EI}(T_s - T) \tag{11}$$

$$\frac{T}{T_s} = 1 - \frac{\sigma_f}{A_{LT}}\left[1 + \ln\left(\frac{\sigma_{LT}}{\sigma_f}\right)\right] \tag{12}$$

In Eqs. (11) and (12), A_{EI}, A_{LT}, and σ_{LT} are fitting parameters. T_s is a critical temperature at or above which the flow stress does not decrease any more upon a further increase of the temperature. For bcc W, $T_s =$ 1000 K is used here. By embedding the dislocation line within an infinite continuum media, Eqs. (11) and (12) may fit well into the experimentally characterized temperature dependence of the flow stress at the macroscopic level. However, they may not be directly applicable to the samples under consideration in the present simulations, where a PBC has been imposed. The PBC-induced image stresses, noted as σ_{img}, cannot simply be ignored. In this scenario, we argue that Eqs. (11) and (12) can be corrected as below by taking the effects of σ_{img} into account, i.e.,

$$\sigma_f^{1/2} = A_{EI}(T_s - T) + \sigma_{img}^{1/2} \tag{13}$$

$$\frac{T}{T_s} = 1 - \frac{\sigma_f - \sigma_{img}}{A_{LT}}\left[1 + \ln\left(\frac{\sigma_{LT}}{\sigma_f - \sigma_{img}}\right)\right] \quad (14)$$

This correction is built upon two arguments. First, the applied stress and the image stress superpose additively to affect the dislocation mobility. Second, for the same simulation cell containing a dislocation line with the same length, the image stresses in the LT and EI regimes are the same. Although the dislocation line morphology in those two regimes differs and might introduce a different σ_{img}, it is considered to play a less important role than that of the dislocation line length in controlling the level of σ_{img}. Fitting of Eqs. (13) and (14) into the FT-CG simulation data in both EI and LT regimes leads to the solid and the dash lines, respectively, in Fig. 8a. This in turn, enables a calibration of the model parameters, A_{EI}, A_{LT}, and σ_{LT}; as well as a characterization of the dislocation line length dependence of A_{EI}, A_{LT}, σ_{LT}, and σ_{img} as listed in Table1 (Proville-EAM) and Table 2 (AT-EAM), respectively, where A_{LT}, σ_{LT}, and σ_{img} are all normalized by σ_0. Finally, it facilitates us to quantify the stresses, σ_{img}, induced by the periodic images of the kinked dislocation lines. Here σ_0 is the critical stress at which the kink starts to appear at $T = 0$ K.

When the Proville-EAM potential is used, four primary findings can be drawn from the data in Table 1. First, the kink nucleation stress, σ_0, at 0 K decreases when the dislocation line length, L, increases from 60 nm to 1 μm. This implies easier kink activation on a longer dislocation. Second, A_{EI} is nearly doubled when L changes from 60 nm to 1 μm. According to Eq. (13), this suggests that, upon the same temperature increase, the flow stress resulting from the motion of a long dislocation lines reduces significantly faster than that of the short dislocation. Third, the level of image stress induced by the periodic kinked dislocation in bcc W may be as high as $0.79\sigma_0$, i.e., ~1.6 GPa, if only a nanometer-long dislocation line is considered but can be significantly reduced to ~0.8 GPa when the dislocation line length is 1 μm. This is reasonable because the kink-kink interaction is inversely proportional to the separation between them. Upon the increase of L, the average spacing between kinks and their periodic images increases, which leads to decreasing interactions, and in turn, a reduction of σ_{img}. This finding suggests that, when L exceeds 1 μm and beyond, the effects induced by the image stresses may be largely reduced. At those length scales, the FT-CG simulation should approach a recovery of the continuum-level EI and LT models in Eqs. (11) and (12). We have performed the relevant large-scale FT-CG simulations and will report the results in a separate publication. By contrast, when the double-humped AT-EAM potential is used, the resulting model parameters (Table 2) exhibit even more obvious line length dependence compared to that evident in Table 1.

3.7. Temperature-, Stress- and Length-dependence of kink activation enthalpy / volume

The observed temperature dependence of the flow stress provides us with the opportunity to deduce two other important quantities, the kink activation volume (ΔV) and activation enthalpy (ΔH), as well as their sensitivity to temperature, stresses, and dislocation line lengths. It should be noted that, in theory, ΔH differs from the kink activation energy, ΔG. By definition, ΔG corresponds to the free Gibbs energy required for displacing one segment of a dislocation line to the next Peierls valley. It is composed of ΔH together with an entropic term (noted as ΔH_T), i.e., $\Delta G = \Delta H - \Delta H_T = \Delta H - T\Delta S$, in which the term of $T\Delta S$ may be evaluated using the Schoeck's correction [96]. In general, ΔH may be quantified using three different approaches: **(i)** the nudged elastic band (NEB) method [27] to determine the reaction pathway and then the energy barrier required for the kink activation on a dislocation line under the action of finite stresses at zero temperature; **(ii)** quantifying the activation parameters through measuring the change of the plastic strain rates on "temperature jumps" when the material is subject to a constant stress. This approach needs the simulation or experiments to be conducted at a relatively long duration, which could be well beyond the reach of MD or the FT-CG simulations; or **(iii)** calculating ΔH according to the following Eq. (15) through measurement of the change of the critical stress, σ_c, i.e., the stress at which the kink starts appearing on a dislocation line, upon "temperature jumps" [97] in a sample under a constant strain-rate deformation, i.e.,

Table 1
EI and LT model parameters fitted from FT-CG simulation (512 atoms per FE) results and their line length dependence (Proville-EAM).

	$\sigma_0(GPa)$	$A_{EI}(\mathrm{MPa}^{1/2}/K)$	A_{LT}/σ_0	σ_{LT}/σ_0	σ_{img}/σ_0
L = 60 nm	2.12	0.0041	0.41	0.48	0.79
L = 150nm	2.05	0.0052	0.63	0.77	0.68
L = 1000nm	1.96	0.0072	0.88	0.80	0.43

Table 2
EI and LT model parameters fitted from FT-CG simulations (512 atoms per FE) results and their line length dependence (AT-EAM).

	$\sigma_0(GPa)$	$A_{EI}(\mathrm{MPa}^{1/2}/K)$	A_{LT}/σ_0	σ_{LT}/σ_0	σ_{img}/σ_0
L = 60nm	2.50	0.0016	2.05	2.39	0.01
L = 150nm	2.46	0.0024	1.20	1.15	0.01

$$\Delta H = -T\Delta V\left(\frac{\partial \sigma_c}{\partial T}\right)_{\dot{\varepsilon}} \quad (15)$$

$$\Delta V = \frac{k_B T \ln(\dot{\varepsilon}_2/\dot{\varepsilon}_1)}{\Delta \sigma_c} \quad (16)$$

Here, ΔV is the kink activation volume and is calculated through the simulations of a series of "strain-rate jump tests". The third approach is employed here to compute ΔV and then ΔH. It has been shown that the activation parameters obtained from such an approach can be consistent with that from static simulations [32,33]. As an approximation to the activation analysis in experiments, FT-CG simulations of the strain-rate and temperature jump tests are composed of two components: **(1)** first, for the sample subjected to deformation under three different strain rates (1.5×10^8/s, 3.0×10^8/s, and 5.0×10^8 /s) at a given temperature, the change of the critical stresses, noted as $\Delta\sigma_c$ in Eq. (16), caused by "the strain-rate jump" is measured and used to calculate the activation volume, ΔV. Such strain-rate jump tests are performed at different temperatures, T = 100 K, 200 K, 400 K, 600 K, 800 K, and 1000 K. At each temperature, σ_c at 3.0×10^8 /s and the ΔV when the strain-rate 'jumps' from 1.5×10^8 /s to 5.0×10^8 /s are recorded and archived in a ΔV-σ plot (Fig. 9a).The data is then used to calibrate the ΔV-σ relation, Eq. (17); **(2)** for the sample subject to a loading at a certain constant strain rate (3.0×10^8 /s) but exposed to different temperatures (T = 100 K, 200 K, 400 K, 600 K, 800 K, and 1000 K), the change of the critical stresses caused by "a temperature jump" is measured as $\partial\sigma_c/\partial T$ via numerical differentiation of the data in Fig. 8a. The values of ΔV obtained in the first step together with the $\partial\sigma_c/\partial T$ are then used in Eq. (15) for calculating ΔH at different temperatures. At each T, the values of σ_c in Fig. 8a and the values of ΔH obtained here are archived in a ΔH-σ plot (Fig. 9c–f). It in turn, can be used to calibrate the ΔH-σ relation, in Eq. (18), derived from the LT theory [95], or the widely-used Kocks relation [26], Eq. (19), used in dislocation dynamics [45–49] or CPFE simulations [27,54–56].

$$\Delta V = A_v \ln\left(\frac{\sigma_v}{\sigma}\right) \quad (17)$$

$$\Delta H^{LT} = H_0^{LT} - \frac{\sigma}{A_H}\left[1 + \ln\left(\frac{\sigma_H}{\sigma}\right)\right] \quad (18)$$

$$\Delta H^{Kock} = H_0^{Kock}\left[1 - \left(\frac{\sigma}{\sigma_0}\right)^p\right]^q \quad (19)$$

Here, A_v,σ_v,A_H, σ_H,H_0^{LT},H_0^{Kock}, p, and q are model parameters; σ_0 values

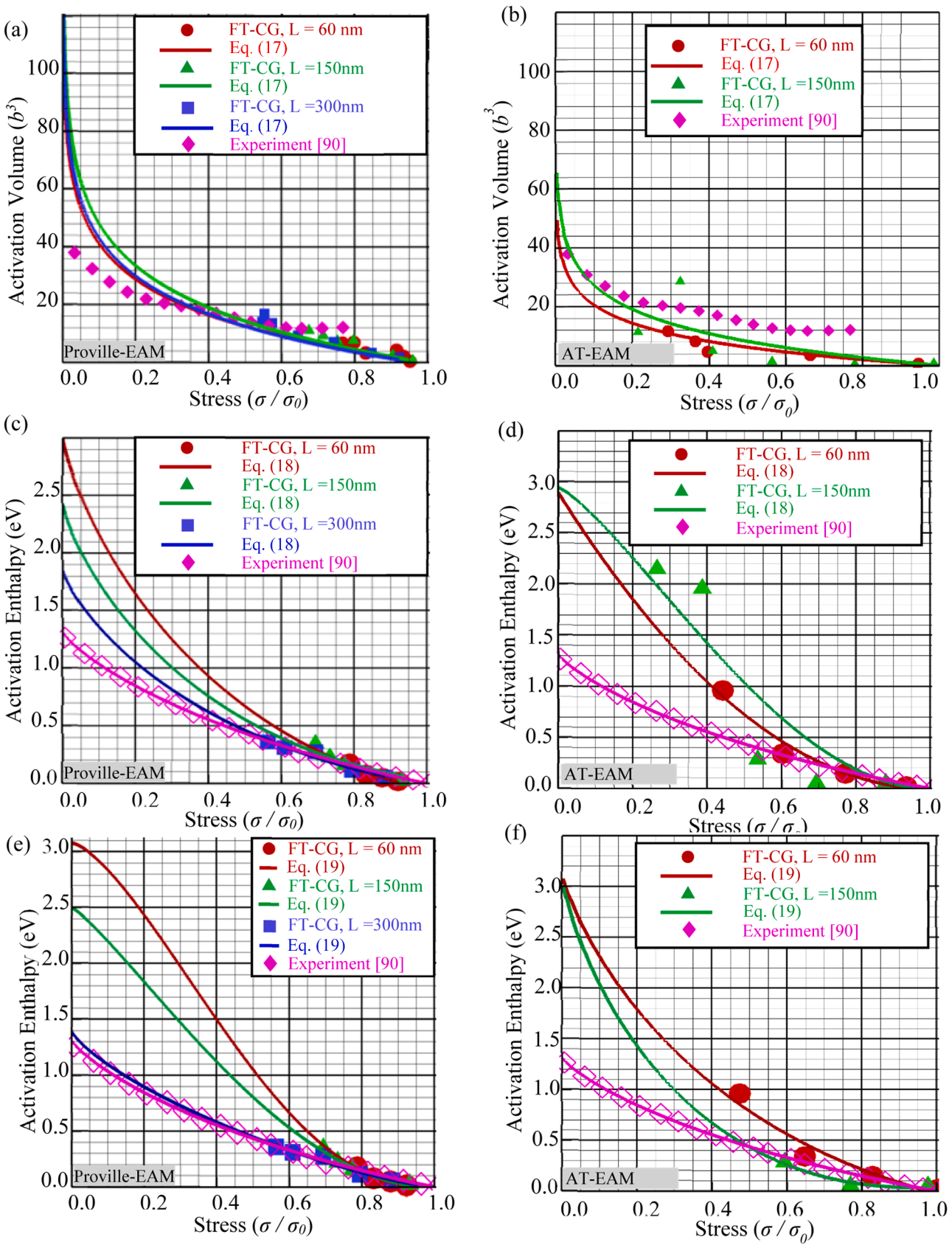

Fig. 9. Activation volume (ΔV) together with the activation enthalpy (ΔH) extracted from FT-CG models (512 atoms per FE) using Proville- and AT-EAM potentials for simulating the motion of a single dislocation line with a length of L in "strain-rate/temperature jump tests" and their comparisons with experimental data: (a, b) the relation between ΔV and the external stress, σ; (c, d) the $\Delta H - \sigma$ relation and its fitting into the LT and (e, f) the Kocks models, respectively. Here, the markers indicate the raw data from simulations and experiments. The solid curves are from a fitting of those raw data into Eqs. (17), (18), and (19), respectively.

are listed in Table 1

Fig. 9 presents the ΔV and ΔH extracted from FT-CG simulations of the motion of a single dislocation line in a bcc W under a series of strain-rate and temperature jump tests. Both the single-hump Proville-EAM and the double-humped AT-EAM potentials are tested here for comparison purposes. Three different dislocation line lengths, $L = 60$ nm, 150 nm, and 300 nm are considered. The fitting of the FT-CG simulation-based data (markers) into the LT and Kocks models is shown as solid curves. As a validation, the data from the activation analysis in experiment [90,91] is also included here. Two major findings emerge from Fig. 9a, b. First, the results are consistent with experimental observations in that the FT-CG simulations predict a decrease of the activation volume and enthalpy upon an increase of stresses. Second, although the current FT-CG simulations only produce the data in high-stress regime ($\sigma / \sigma_0 > 0.5$), the simulation-based ΔV and ΔH in this regime quantitatively agree very well with the experimental results.

A fitting of the simulation and experimental data using the LT and Kocks models (curves in Fig. 9) shows: **(a)** through a fitting of the data from high-stress FT-CG simulations according to the LT or Kocks models, the ΔV and ΔH for the kink activation on a single dislocation line subjected to a high stress are found to be comparable with that from experiments, but significantly diverge from experimental results at low stresses. For instance, at $\sigma \to 0$, the ΔV based on the fitting of the FT-CG simulations into the LT model is $\sim 100b^3$. In contrast, $\Delta V \approx 40b^3$ in experiments at $\sigma \to 0$ (Fig. 9a). Similarly, for kink activation on a 60nm-long dislocation line, the ΔH at $\sigma \to 0$ resulting from fitting the FT-CG simulation data into the LT (Fig. 9c) and the Kocks model (Fig. 9e) is ~3.0 eV, which is two times larger than that, ~1.4 eV, in experiments (Fig. 9e). Such a difference between FT-CG and experiments is amplified if a double-humped AT-EAM potential (Fig. 9b, d, f) is used due to an extended reaction pathway of uncorrelated leading and trailing kink pairs.; **(b)** the FT-CG simulation-based ΔV-σ relation in the high-stress regime ($\sigma / \sigma_0 > 0.5$) exhibits no dependence on L, i.e., the ΔV-σ relations for $L = 60$ nm, 150 nm, and 300 nm nearly overlap with each other (Fig. 9a). As such, the fitted LT models for the ΔV-σ relation do not exhibit an obvious dependence on L either (Fig. 9a); **(c)** the FT-CG simulation-based ΔH-σ relation in the high-stress regime ($\sigma / \sigma_0 > 0.5$) exhibits a dependence on the dislocation line length, i.e., a lower ΔH on a larger L, which again implies a relatively 'easier' kink activation on a longer dislocation line. The L-dependence of the ΔH-σ relation can be even amplified in the low-stress regime if one follows the LT (Fig. 9c) and Kocks model (Fig. 9e). Similar to the temperature dependence of the flow stress in Fig. 8a, when L increases from 60 nm to 300 nm, the FT-CG simulation-based ΔH-σ relation is closer to that from experiments (Fig. 9c, e). In particular, a fitting of the ΔH-σ data from FT-CG simulations for $L = 300$ nm into the Kocks model agrees well with experiments (Fig. 9e).

The knowledge gained above facilitates the utilization of FT-CG to calibrate the LT and Kocks models, especially the dislocation line length dependence of the model parameters. This is non-trivial for experiments because it is difficult to measure the kink activation on a single dislocation line. Such information is, however, required by reduced order continuum computer simulations, such as DD or CPFE, where the activation events occur on dislocation lines with a variety of lengths ranging from tens of nanometers to several microns. As a preliminary attempt along this direction, Table 3 lists the model parameters obtained from fitting the Proville-EAM potential-based FT-CG simulation data (Fig. 9a, c, e) into the LT and Kocks models, i.e., Eq. (17), Eq. (18), and Eq. (19), respectively. It is seen that the data obtained from fitting our FT-CG simulation results into the Kocks-Argon-Ashby model, e.g., $H = 1.40$ eV, $p = 0.80$, and $q = 1.3$ when $L = 300$ nm, are reasonably comparable with that ($H = 1.63$ eV, $p = 0.86$, and $q = 1.69$) and ($H = 1.68$ eV, $p = 0.83$, and $q = 1.38$) from atomistic calculations in [23] and [38], respectively.

Several findings from Table 3 can be summarized: **(i)** the data regarding the ΔH-σ relation from the experiments conforms to both the LT and Kocks models very well, which gives to nearly the same kink activation enthalpy at zero external stresses, i.e., $H_0 = 1.32$ eV in the LT model and $H_0 = 1.30$ eV in the Kocks model, respectively; **(ii)** the FT-CG simulation-calibrated values for the parameters of A_H, p, q, as well as H_0 for both the LT and Kocks models exhibit an obvious dislocation line length dependence. They converge towards the experimental value when L increases from 60 nm to 300 nm. In particular, when $L = 300$ nm, the Kocks model parameters ($H_0 = 1.40$ eV, $p = 0.8$, $q = 1.3$) extracted from FT-CG simulations are nearly the same as those values ($H_0 = 1.30$ eV, $p = 0.8$, $q = 1.4$) obtained from experiments. Therefore, although the function forms of ΔH in Eqs. (18) and (19) are phenomenological in nature, they provide a reasonably good description on the kink activation energy as a function of the stress, σ. The values of those exponents, p and q, obtained here for the Kocks model are at the same level as that by isotopic linear elasticity and those used in DD simulations [45–49]; **(iii)** by contrast, A_v, σ_v, and σ_H fit from FT-CG simulations do not change much upon the increase of L. In principal, σ_v, and σ_H should be the same as σ_{LT} in Table 1 if an appropriate correction as included in Eq. (14) is also introduced in Eqs. (17)–(19) for taking the image stress, σ_{img}, into account. A reasonable fitting of the σ_{img}-adjusted LT and Kocks models in Eqs. (17)–(19), however, demands data from additional FT-CG simulations of "strain-rate and temperature jump tests" in the low-stress regime. Because the kink-pair activation at low stress is a rare event, it can be only captured in long-time simulations and may be achieved by combining FT-CG, NEB, and kinetic Monte Carlo (kMC) simulations. This is discussed in the summary section of this paper and will be attempted in the future. The data in Table 3 also suggest that, when the dislocation line length falls into a range between tens and hundreds of nanometers, ΔV and ΔH for the kink dynamics along the dislocation line need to be carefully quantified according to its length, L, and the local stress, σ, acting on it. The result from macroscale experimental can be only considered as an average measurement resulting from a collective behavior of many micrometer-long dislocations along favorable slip planes. The quality of the fitting process that incorporates our present FT-CG simulation results into Eqs. (17)–(19) is promising. If desired, the same procedure can be repeated for an ensemble of simulations with a large number of different line lengths being considered. This will enable us to extract a functional form of the L-dependent model parameters, i.e., H_0 (L), A_H (L), p (L), and q (L), which will be useful in higher length-scale simulations.

In addition to the determination of a stress dependence of ΔH, the constant strain-rate FT-CG simulations can be also used to characterize the temperature dependence of ΔH_T (the entropic term that contributes to kink activation). According to the well-known Orowan equation, as a response to the loading at a constant strain rate $\dot{\varepsilon}$ (the plastic strain rate dominates here), the screw dislocation line will glide at a constant velocity, Vs. Moreover, according to the LT theory in Eq. (1), the velocity of a dislocation with a certain length, Vs, is proportional to $exp[-\Delta H_T /$

Table 3
The LT and Kocks model parameters fitted using FT-CG simulations and experimental data [90].

	$A_v(b^3)$	σ_v/σ_0	A_H(MPa /eV)	σ_H/σ_0	H_0^{LT}(eV)	H_0^{Kock}(eV)	p	q
$L = 60$ nm	18	1.01	949	1.42	2.94	3.08	1.5	2.4
$L = 150$nm	21	0.99	1153	1.45	2.42	2.50	1.2	2.0
$L = 300$nm	19	0.97	1513	1.50	1.85	1.40	0.8	1.3
Experiments	8	1.50	1544	3.07	1.32	1.30	08	1.4

(k_BT)]. Mathematically, these arguments can be expressed as Eq. (20). According to Eq. (20), when the steady-state dislocation motion at a constant of $\dot{\varepsilon}$ is achieved, ΔH_T will be linearly proportional to k_BT, i.e., Eq. (21). With an MD-comparable timesteps during the time integration, the strain rates (10^8/s) deployed in the present FT-CG simulations are significantly higher than that (10^{-4}/s) in experiments. Thus, when a validation of the FT-CG simulation-based ΔH_T - T relation is undertaken, the strain-rate differences between simulations and experiments need to be taken into account as shown in Eq. (22) according to [32]. Here, ΔH_T and ΔH_T* represent the values directly extracted from FT-CG simulation and the 'corrected' activation enthalpy, respectively.

$$V_s \propto \dot{\varepsilon} \propto \exp\left(-\frac{\Delta \mathrm{H}_T}{k_BT}\right) \tag{20}$$

$$\Delta \mathrm{H}_T = Ck_BT \tag{21}$$

$$\Delta \mathrm{H}_T^* = \Delta \mathrm{H}_T + k_BT \ln\left(\frac{\dot{\varepsilon}_{\mathrm{sim}}}{\dot{\varepsilon}_{\mathrm{exp}}}\right) = C^* k_BT \tag{22}$$

Fig. 10 presents the ΔH_T -T relation characterized from the Proville-EAM potential-based FT-CG simulations of the motion of a single dislocation line in bcc W and its fitting into Eqs. (21) and (22). The results from experiments [90,91] are also included in Fig. 10 for validation purposes. Here, the computed ΔH_T are indicated as markers, which are calculated according to Eq. (15) through a series of FT-CG simulations at five different temperatures (T = 100 K, 200 K, 400 K, 600 K, 800 K, and 1000 K). Again, three dislocation line lengths (L = 60 nm, 150 nm, and 300 nm) are considered. Several major findings in Fig. 10 are: **(i)** the data from the FT-CG simulations obeys the linear ΔH_T - T relationship regardless of dislocation line length; **(ii)** the slope C in Fig. 10a of the ΔH_T - T relationship exhibits a clear dependence on the dislocation line length, i.e., a higher slope is observed on a longer dislocation. For instance, $C \approx 7$ for L = 300 nm but $C \approx 2$ for L = 60 nm; **(iii)** with an increasing L, the simulation-based ΔH_T - T relationship approaches but still largely deviates from the experimental results (Fig. 10a) unless a strain-rate based correction, Eq. (22), is introduced (Fig. 10b); and **(iv)** the FT-CG simulation-based $\Delta \mathrm{H_T}$ -T relations with such a 'correction' are quantitatively comparable with that from experiments (Fig. 10b). Experimentally, the ratio (noted as C and C* in Fig. 10) between ΔH_T and k_BT, is found to be ~20 for potassium and about 23~27 for bcc transition metals [32]. Clearly, under the correction, the results from high-rate FT-CG simulations of the motion of long dislocation line can be very close to, although not exactly the same as, that from experiments (Fig. 10b).

3.8. *Atomistic mechanisms underlying the motion of μm-long dislocations in bcc metals*

Although the exact one-to-one correspondence between simulations and experiments is not yet achieved yet owing to neglect of microstructure complexity, quantum effects, and number of other factors discussed earlier, an increase of L to 1 μm in FT-CG still largely expands the predictive capability of atomistic simulations to inform higher length scale models. It not only enables simulation results to get one step closer to that of experiments, as shown in Figs. 8–10, but also can provide the atomistic mechanisms underlying the kink-controlled motion of the μm-long dislocations as shown below, because the atomistic information naturally undergirds FT-CG.

Fig. 11a presents the time sequence of the local stress evolution on the slip plane, along which the initial dislocation line migrates, in a bcc W sample under a shear stress of 3.70 GPa from Proville-EAM-based FT-CG simulations at temperature T = 1000 K. The FE simulation discretizes this sample (containing ~94 million atoms) into 184,000 coarse elements (512 atoms per FE). the FE nodal displacements are direct outputs from FT-CG simulations. Here, the FE configuration and the local strain and stress distributions are calculated from the FE nodal displacements through a routine post processing procedure. Moreover, as mentioned before, because each FE in FT-CG models is embedded with a collection of atoms, the reconfigurations of those atoms within the sample under deformation can be mapped from FE nodal displacements through the tri-linear shape functions. The dislocation core structure and its evolution can be then extracted from the fully atomic configuration through a centro-symmetry parameter or coordination number analysis (Fig. 11b). Without the need to explicitly solve for the motion of each atom, our FT-CG simulations successfully capture three signature events associated with the atomistic kink activities along the μm-long dislocation lines which are often observed in the experiments on bcc transition metals under deformation at low temperature [1–4,98]: **(1)** first, assisted by thermal fluctuations, many small portions of the long dislocation line 'jump' to the next Peierls valley forming kinks (t = 10 ps in Fig. 11b); **(2)** these kinks migrate along the dislocation line and collide with each other. As a consequence of such collisions, the dislocation line becomes corrugated by developing 'cross-kinks' (t = 20 ps in Fig. 10b) and then the vacancy loops (t = 30 ps in Fig. 11b). They occur on the FE boundaries in FT-CG. Consistent with the results from the full MD simulations in [31], here the loop forms through shifting atomic rows along the dislocation line; and **(3)** at a higher stress, the dislocation line breaks away from these self-pinning points, which results in a jerky dislocation motion. Meanwhile, the vacancy loop left behind is closed (t = 40 ps in Fig. 11b). Clearly, although at a lower resolution than that of full MD due to the use of a coarse-graining process through FE, the FT-CG retains

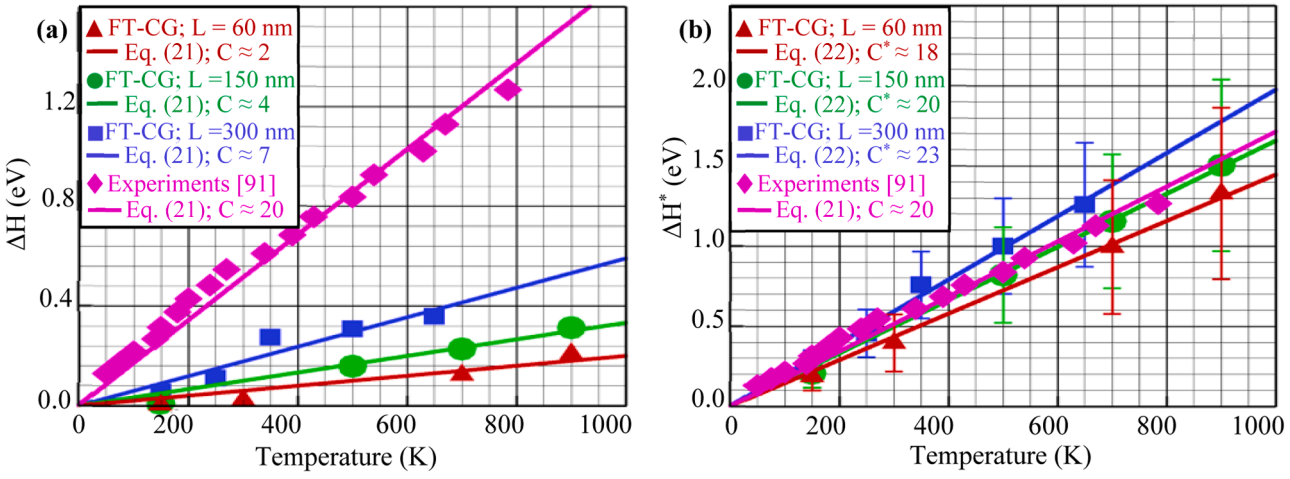

Fig. 10. $\Delta \mathrm{H_T}$ obtained from FT-CG (512 atoms per FE) and its fitting into (a) Eq. (21); and (b) Eq. (22).

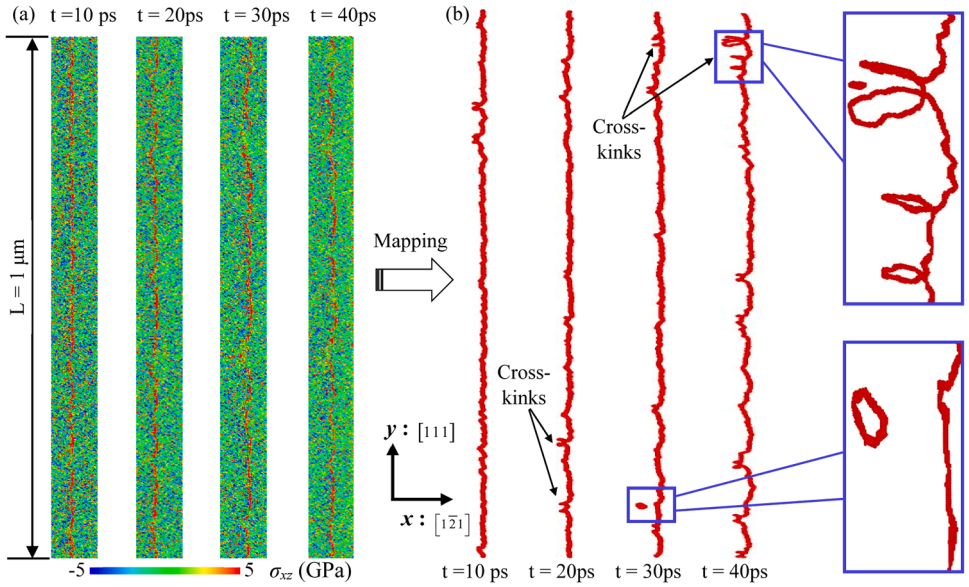

Fig. 11. Mechanisms revealed by the FT-CG (512 atoms per FE) for the motion of a μm-long dislocation line in bcc W under a shear stress of 3.7 GPa at $T = 1000$K: **(a)** time sequences of the local stress evolution on the deformed FE mesh configuration, from which the dislocation line and its migration on the slip plane can be clearly recognized; **(b)** time sequence of the atomic-level core structure evolution on the dislocation line mapped from the FE configuration without the need of explicitly solving for the motion of each atom.

the atomistic essentials of the kink-controlled dislocation dynamics.

More importantly, given its capability to address dislocations with lengths at the micrometer level, it is expected that the FT-CG simulation results will enrich the database to be used for calibrating the dislocation mobility laws with a full-spectrum characterization of their dependences on the line lengths. It can provide us with useful information regarding dislocation line length effects, beyond temperature and stress effects that are commonly considered in full MD [31]. This in turn, can be used to construct deformation mechanism maps for understanding the kink-controlled dislocation dynamics. For instance, MD simulations [31] show that the nm-long dislocation in bcc metals becomes rough at considerably high stress and high temperature. Through scaling the dislocation line length up to micrometers, with a high-quality interatomic potential being used as the constitutive rule, the FT-CG can be used to test one hypothesis: the dislocation line in high-Peierls-barrier materials can be also rough even at very low stress and low temperature as long as it is sufficiently long. As a preliminary attempt along this direction, we have performed FT-CG simulations with the dislocation length scaling up to 5μm-10 μm and will report the relevant results separately.

4. Summary and discussion

The plastic flow in bcc transition metals under deformation at finite temperature clearly occurs across a wide range of length scales, because the motion of μm-long screw dislocations together with the atomic-scale processes of kink nucleation and propagation along those dislocations. Although the kinks are atomistic entities, their effects on dislocation motion can extend to very long range [41]. Hence, the behavior of μm-long dislocations differs substantially from that of the short segments which have commonly considered in MD. Exploring the full parametric space of the line length dependence of the dislocation mobility law necessitates an approach that can explicitly incorporate the atomic-sized kinks into the description of the motion of long dislocations. Here we advance a FT-CG approach to address this need. The FT-CG approach is the FE implementation of a unified atomistic and continuum description of materials that extends the Irving-Kirkwood procedure [70–72] in statistical mechanics. It expands our previous CG model [57–63] for dislocation dynamics in fcc crystals through equipping it with **(i)** new FEs to realize a CG description of dislocations in bcc transition metals, which not only requires a much less cost than that by full MD but also retains the non-planar atomistic core structure along the dislocation line; and **(ii)** a phonon dynamics-based finite temperature algorithm to resolve the full spectrum of the crystal's lattice dynamics without cutting off short-wavelength phonons as is the case for many other CG approaches.

Taking bcc W as a model material, we then demonstrate the FT-CG capability to characterize the kink dynamics on a single ½<111> screw dislocation line as a function of stress, temperature, and most importantly, line length ranging from nanometers to microns. Two novel aspects of the FT-CG model are: **(a)** both the enthalpy and the vibrational entropy associated with kink-pair formation have been included into this model, where the enthalpic component has been shown to map well with a LT or Kocks model and the entropic contribution can match reasonably well with the temperature dependence of the flow stress; **(b)** it has an atomistic resolution for the kink formations and interactions, even on very long dislocation. Here we have considered several typical line lengths: ~ 60 nm as the commonly used length in many existing MD simulations; ~150nm-300 nm near the limit of what can be simulated in MD at a maximum computing resource available to us; and ~1 μm near the average dislocation lengths in well-annealed bcc W crystals.

Through FT-CG simulations of the motion of a single dislocation line in strain-rate and temperature jump tests, our major findings are: **(1)** at a much lower cost than that of full MD, the FT-CG predicts not only the PDoS degeneration caused by the lattice distortion near a dislocation core, but also the atomic-level "soft-to-hard" core structure transition induced by the kink activities on the μm-long dislocation line; **(2)** the flow stress-temperature (σ_f-T) relation exhibits a strong dependence on the dislocation line length, L. When L increases from 60 nm to 1 μm, the simulation-predicted σ_f–T is closer to that from experiments. Upon the same level of temperature increase, the reduction of the flow stress associated with the motion of μm-long dislocations is significantly greater than that associated with the motion of nm-long dislocations; **(3)** the "knee temperature" (noted as T_k), i.e., the transition temperature between the LT and EI regimes in the σ_f-T relation is insensitive to L. For all the dislocation line lengths considered here, the FT-CG predicts an experimentally comparable $T_k = 600$ K, which corresponds to the BDT transition temperature. This suggests that the kink dynamics crossover

from LT to EI may be one mechanism responsible for the BDT; **(4)** the enthalpy-stress (ΔH-σ) relation exhibits a non-linear dependence on L. An experimentally comparable H_0 at ~1.4 eV (kink activation enthalpy at $\sigma = 0$) can be estimated when $L = 300$ nm but can be as high as ~3.1 eV when $L = 60$ nm if the Kocks model is employed for fitting the FT-CG simulation results. This suggests an easier kink activation on a longer dislocation line. Such a dislocation line length dependence of the kink activation enthalpy can be further amplified with the decrease of the applied stress; **(5)** the relation between the entropic kink activation and the temperature, i.e., the ΔH_T -T relation, also exhibits a dependence on the line length, L. For bcc W under the high strain-rate deformation, the FT-CG simulation-predicted ΔH_T of ~$7k_BT$ when $L = 300$ nm but ~$2k_BT$ when $L = 60$ nm, although both of which can get closer to that, $20k_BT$, from low strain-rate experiments if a strain-rate-based correction is introduced; **(6)** the critical stress/temperature required for the occurrence of cross-kinks, self-pinning, vacancy loop production and closure on a μm-long dislocation line can be significantly lower than that on a nm-long lines.

The above findings will lead to: **(i)** a calibration of the dislocation line length dependence of the parameters of the LT and Kocks models from the atomistic scale up to the micrometer level and even above**; (ii)** the formulation of the new dislocation mobility law that unifies the temperature-, stress-, as well as the complex dislocation line length-dependence all in one closed form for line lengths spanning a wide range from tens of nanometers to microns; **(iii)** the construction of a deformation mechanism map that correlates the dislocation roughening processes, velocities, stresses, temperatures, and the dislocation line lengths with each other. Through incorporating such knowledge into the higher length scale models, e.g., DD [45–49], phase field (PF) [50–53], or CPFE [27,54–56], a prediction of the plastic flow in bcc transition metals at an experimentally comparable length scale may be achieved. In particular, an intended utilization of the comprehensive mobility law in DD may largely improve its predictive capability for modeling the dislocation microstructure evolution in plastically deformed bcc metals since such mobility laws will be based on atomistic mechanisms and will span a broad range of length scales. These mobility laws may enable an introduction of the fewest number of degrees of freedom while still accurately capturing the dynamics of long dislocation lines. Such atomistic-to-mesoscale simulation-based mobility laws may expand the predictive capability of DD to better inform macroscale relations. It can then facilitate a transfer of the DD-based microstructure evolution to CPFE for describing the plastic flow in bcc metals at the macroscale. For instance, the flow rules that connect the shear strain rate on a given slip system in bcc metals under deformation at finite temperature with the stress on that slip system can be better formulated. The resulting CPFE model, if furnished with the rules for the interactions between slip and grain boundaries, may provide researchers with a steppingstone to better understanding plastic flow in polycrystalline bcc metals and many other high-Peierls-barrier materials at the grain scale when exposed to extreme environments (stress, temperature, irradiation, corrosion, or some combination).

Despite its potential to fill gaps between various single-scale computational models, experiments, and theories, one, however, has to be cautious about the present FT-CG simulation results in several respects:

(1) in bcc crystals, not only the shear stress but also the other stress components all play important roles in controlling the dislocation mobility. When a bcc crystal is subjected to a general stress tensor, cross-slip can easily occur. The incorporation of such a so-called non-Schmid effect [99–101] into the computer simulations is critical to modeling atomic-level cross-slip and the mesoscopic-level tension-compression asymmetry for being fully consistent with experimental observations. The element set-up in the present FT-CG only considers dislocation motion on only the {110} slip planes, but not the {112} and {123} planes, along the element boundaries. It thus does not accommodate all the possible slip activity involved in dislocation cross-slip. A tetrahedral- rather than the rhombohedral-shaped element should be able to satisfy this need and is under development in our group. The preliminary results from our recent FT-CG simulations equipped with such a newly developed are promising and show that the compressive and tensile stresses, σ, along the normal direction of the dislocation gliding plane can promote and suppress the mobility of dislocations in bcc metals, respectively.

(2) in this work, the kink-pair activation barrier is extracted from dynamical, constant strain-rate FT-CG simulations. The obtained ΔH-σ or ΔH_T - T relation indeed follows the same trend as that from experiments, but the magnitude of ΔH at low stress has not been measured in FT-CG simulations yet. One main reason is the limited time scales of the current FT-CG approach. To accurately determine the activation parameter that dictates the stress-driven kink formation process along μm-long dislocation lines, an integration of the NEB method [27] with the current computational framework and kinetic Monte Carlo (kMC) simulation is necessary. This can be achieved three main steps: (a) performing dynamic FT-CG simulations of the motion of a μm-long dislocation motion under high stresses for a duration of nanoseconds. Although the dynamics of dislocations has been overdriven by the unrealistically high stresses, such simulations will provide us with the database of the metastable configurations for a long dislocation line when multiple kinks are activated; (b) calculating the energy barrier, ΔE (σ), in NEB by using the smooth and kinked dislocation line as the initial and final configuration, respectively, and then the attempting frequency for the kink activation on a long dislocation line through $\upsilon = \upsilon_0 \exp(-\Delta E / k_BT)$; (c) creating a catalog of ΔE and υ accessible to kMC, and then performing kMC simulations at a significantly longer time scales. The reason that kMC can scale up in time is because the attempting frequency of rare events (high ΔE) will be very low. All the physically favorable (low ΔE) kink configuration will be effectively captured by kMC. The strain-rate jump tests will be then performed through FT-CG-informed kMC simulations with both length and time scales comparable to that in experiments.

(3) similar to nearly all the existing atomistic simulations [14,15,20–23,30–39,92], the Peierls stress estimated from FT-CG is by a factor of 3 or more that from experiments [92]. As documented in the literature, this discrepancy between experimental and calculated Peierls stresses could arise from the absence of the quantum effects [6], the inaccuracy of the interatomic potential [76], the exclusion of the effects from a variety of other material defects such as solute atoms, interstitial impurities, non-screw dislocations near the source, grain boundaries, and the ignorance of the complex local stresses induced by those defects in simulations [6,92]. In principle, the effects of all these factors on the dislocation motion might be incorporated into our FT-CG framework. For instance, the quantum effects might be approximately considered through replacing the traditional interatomic potential with a high-fidelity machine learned interatomic potential [86,94].

(4) in this work, we focus on coarse graining only by using a uniform FE mesh to discretize the whole sample. The FEs around the dislocation core are in the same size as those far away from it. There is no atomistic domain in our CG model and thus no spurious heating induced by the high-frequency and short-wavelength phonon reflection-induced spurious heating. If a characterization of the effects of the temperature on the interaction between dislocations and other materials defects, such as voids, stacking fault tetrahedra, and grain boundaries, is desired, there will be a need to combine present FT-CG model with the atomistic description of those defects into one framework. This will result in a finite temperature concurrent atomistic-

continuum (FT-CAC) model. In such FT-CAC simulations, we need to assure a smooth passage of high-frequency phonons from atomistic to coarse domains [102,103]. This has been attempted in our previous work [104,83] using a one-dimensional (1D) computational set-up. One main idea there is to accommodate the short-wavelength/high-frequency phonons in the CG domain through enriching the linear finite element shape functions with lattice dynamics-based wavelets. Such enrichments can be analytically derived in 1D problems and does enable the high-frequency phonons from the atomistic domain to the CG domain. Despite its great potential, an expansion of it to 3D, however, remains non-trivial. By contrast, imposing the high-frequency phonon-induced vibrations directly on the FE nodes through Eq. (8) in this work may provide us with an alternative vehicle to address this issue. According to our recent results in [69], when equipped with Eq. (8), FT-CG is effective in predicting the thermal expansion and volume change (V/V_0) of bcc metals at finite temperature. As previously suggested Marian and his co-worker in [103], the thermal expansion coefficient may be used as a metric to assess the entropy loss induced by coarse graining because phonons with all different wavelengths/frequencies contribute to thermal expansion. The FT-CAC approach is currently under development and will be reported soon.

Declaration of Competing Interest

The authors declare that they have no known competing financial interests or personal relationships that could have appeared to influence the work reported in this paper.

Acknowledgement

JR, TP, and LX acknowledges the support of the U.S. National Science Foundation (CMMI-2322675 and CMMI-2328533) and the Extreme Science & Engineering Discovery Environment (XSEDE-TG-MSS170003 and XSEDE-TG-MSS190008). DLM is grateful for the support of the Carter N. Paden, Jr. Distinguished Chair in Metals Processing.

References

[1] D. Caillard, Kinetics of dislocations in pure Fe. Part I. *In situ* straining experiments at room temperature, Acta Mater. 58 (2010) 3493–3503.
[2] D. Caillard, An *in situ* study of hardening and softening of iron by carbon interstitials, Acta Mater. 59 (2011) 4974–4989.
[3] D. Caillard, Geometry and kinetics of glide of screw dislocations in tungsten between 95 K and 573 K, Acta Mater. 161 (2018) 21–34.
[4] D. Caillard, A TEM *in situ* study of the softening of tungsten by Rhenium, Acta Mater. 194 (2020) 240–256.
[5] L. Ventelon, F. Willaime, E. Clouet, D. Rodney, Ab initio investigation of the Peierls potential of screw dislocations in bcc Fe and W, Acta Mater. 61 (2013) 3973–3985.
[6] L. Proville, D. Rodney, M.C. Marinica, Quantum effect on thermally activated glide of dislocations, Nat. Mater. 11 (2012) 845–849.
[7] M. Itakura, H. Kaburaki, M. Yamaguchi, First-principles study on the mobility of screw dislocations in bcc iron, Acta Mater. 60 (2012) 3698–3710.
[8] L. Proville, L. Ventelon, D. Rodney, Prediction of the kink-pair formation enthalpy on screw dislocations in α-iron by a line tension model parameterized on empirical potentials and first-principles calculations, Phys. Rev. B 87 (2013), 144106.
[9] L. Dezerald, L. Proville, L. Ventelon, F. Willaime, D. Rodney, First-principles prediction of kink-pair activation enthalpy on screw dislocations in bcc transition metals: V, Nb, Ta, Mo, W, and Fe, Phys. Rev. B 91 (2015), 094105.
[10] C.R. Weinberger, G.J. Tucker, S.M. Foils, Peierls potential of screw dislocations in bcc transition metals: predictions from density functional theory, Phys. Rev. B 87 (2013), 054114.
[11] J.E. Dorn, S. Rajna, in: Proceedings of the Gordon Research Conference, New London, N.H, 1963. July 10-30.
[12] A. Seeger, The kink picture of dislocation mobility and dislocation-point defect interactions, J. Phys. Colloq. 42 (C5) (1981). C5-201-C5-228.
[13] A. Seeger, The temperature and strain-rate dependence of the flow stress of body-centered cubic metals: a theory based on kink-kink interactions, Z. Metallkunde Int. J. Mater. Res. 72 (6) (1981) 369–380.
[14] V.V. Bulatov, J.F. Justo, W. Cai, S. Yip, Kink asymmetry and multiplicity in dislocation cores, Phys. Rev. Lett. 79 (25) (1997) 5042–5045.
[15] A.H.W. Ngan, M. Wen, Dislocation kink-pair energetics and pencil glide in body-centered-cubic crystals, Phys. Rev. Lett. 87 (7) (2001), 075505-14.
[16] M. Tang, L.P. Kubin, G.R. Canova, Dislocation mobility and the mechanical response of bcc single crystals: a mesoscopic approach, Acta Mater. 46 (9) (1998) 3221–3235.
[17] R. Groger, A.G. Bailey, V. Vitek, Multiscale modeling of plastic deformation of molybdenum and tungsten: I. Atomistic studies of the core structure and glide of ½ <111>screw dislocations at 0 K, Acta Mater. 56 (2008) 5401–5411.
[18] R. Groger, V. Racherla, J.L. Bassani, V. Vitek, Multiscale modeling of plastic deformation of molybdenum and tungsten: II. Yield criterion for single crystals based on atomistic studies of glide of ½ <111>screw dislocations, Acta Mater. 56 (2008) 5412–5425.
[19] R. Groger, V. Vitek, Multiscale modeling of plastic deformation of molybdenum and tungsten: III. Effects of temperature and plastic strain rate, Acta Mater. 56 (2008) 5426–5439.
[20] P.A. Gordon, T. Neeraj, Y. Li, J. Li, Screw dislocation mobility in BCC metals: the role of the compact core on double-kink nucleation, Model. Simul. Mater. Sci. Eng. 18 (2010), 085008.
[21] S. Queyreau, J. Marian, M.R. Gilber, B.D. Wirth, Edge dislocation mobilities in bcc Fe obtained by molecular dynamics, Phys. Rev. B 84 (2011), 064106.
[22] M.R. Gilbert, S. Queyreau, J. Marian, Stress and temperature dependence of screw dislocation mobility in α-Fe by molecular dynamics, Phys. Rev. B 84 (2011), 174103.
[23] A. Stukowski, D. Cereceda, T.D. Swinburne, J. Marian, Thermally-activated non-Schmid glide of screw dislocations in W using atomistically-informed kinetic Monte Carlo simulations, Int. J. Plast. 65 (2015) 108–130.
[24] G. Po, Y. Cui, D. Rivera, D. Cereceda, T.D. Swinburne, J. Marian, N. Ghoniem, A phenomenological dislocation mobility law for bcc metals, Acta Mater. 119 (2016) 123–135.
[25] M. Boleininger, M. Gallauer, S.L. Dudarev, T.D. Swinburne, D.R. Mason, D. Perez, Statistical mechanics of kinks on a gliding screw dislocation, Phys. Rev. Res. 2 (2020), 043254.
[26] U.F. Kocks, A.S. Argon, M.F. Ashby, Thermodynamics and Kinetics of Slip, Pergamon Press, Oxford, 1975. *Progress in Materials Science*, 19, eds. B. Chalmers, J.W. Christian, and T.B. Massalski.
[27] S. Narayanan, D.L. McDowell, T. Zhu, Crystal plasticity model for bcc iron atomistically informed by kinetics of correlated kink-pair nucleation on screw dislocation, J. Mech. Phys. Solids 65 (2014) 54–68.
[28] T.B. Britton, A.J. Wilkinson, Stress fields and geometrically necessary dislocation density distributions near the head of a blocked slip band, Acta Mater. 60 (2012) 5773–5782.
[29] Y. Guo, T.B. Britton, A.J. Wilkinson, Slip band–grain boundary interactions in commercial-purity titanium, Acta Mater. 76 (2014) 1–12.
[30] M. Wen, A.H.W. Ngan, Atomistic simulation of kink-pairs of screw dislocations in body-centered cubic iron, Acta. Mater. 48 (2000) 4255–4265.
[31] J. Marian, W. Cai, V. Bulatov, Dynamic transitions from smooth to rough to twinning in dislocation motion, Nat. Mater. 3 (2004) 158–163.
[32] C. Domain, G. Monnet, Simulation of screw dislocation motion in iron by molecular dynamics simulations, Phys. Rev. Lett. 95 (2005), 215506.
[33] J. Chaussidon, M. Fivel, D. Rodney, The glide of screw dislocations in bcc Fe: atomistic static and dynamic simulations, Acta Mater. 54 (2006) 3407–3416.
[34] D. Rodney, Activation enthalpy for kink-pair nucleation on dislocations: comparison between static and dynamic atomic-scale simulations, Phys. Rev. B 76 (2007), 144108.
[35] D. Rodney, L. Proville, Stress-dependent Peierls potential: influence on kink-pair activation, Phys. Rev. B 79 (2009), 094108.
[36] T.D. Swinburne, S.L. Dudarev, S.P. Fitzgerald, M.R. Gilbert, A.P. Sutton, Theory and simulation of the diffusion of kinks on dislocations in bcc metals, Phys. Rev. B 87 (2013), 064108.
[37] N.N. Kumar, E. Martinez, B.K. Dutta, G.K. Dey, A. Caro, Nodal effects in α-iron dislocation mobility in the presence of helium bubbles, Phys. Rev. B 87 (2013), 054106.
[38] S. He, E. Overly, V. Bulatov, J. Marian, D. Cereceda, Coupling 2D atomistic information to 3D kink-pair enthalpy models of screw dislocations in bcc metals, Phys. Rev. Mater. 3 (2019), 103603.
[39] S. Starikov, D. Smirnova, T. Pradhan, Y. Lysogorskiy, H. Chapman, M. Mrovec, R. Drautz, Angular-dependence interatomic potential for large-scale atomistic simulation of iron: development and comprehensive comparison with existing interatomic models, Phys. Rev. Mater. 5 (2021), 063607.
[40] P. Anderson, J. Hirth, J. Lothe, Theory of Dislocations, Cambridge University Press, 2016.
[41] R. Ji, T. Phan, H. Chen, L. Xiong, Quantifying the dynamics of dislocation kinks in iron and tungsten through atomistic simulations, Int. J. Plast. 128 (2020), 102675.
[42] N.M. Ghoniem, S.H. Tong, L.Z. Sun, Parametric dislocation dynamics: a thermodynamics-based approach to investigations of mesoscopic plastic deformation, Phys. Rev. B 61 (2000) 913.
[43] C. Zhou, S.B. Biner, R. LeSar, Discrete dislocation dynamics simulations of plasticity at small scales, Acta Mater. 58 (5) (2010) 1565–1577.
[44] C.R. Weinberger, C.C. Battaile, T.T. Buchheit, E.A. Holm, Incorporating atomistic data of lattice friction into bcc crystal plasticity models, Int. J. Plast. 37 (2012) 16–30.

[45] M. Tang, J. Marian, Temperature and high strain rate dependence of tensile deformation behavior in single-crystal iron from dislocation dynamics simulations, Acta Mater. 70 (2014) 123–129.
[46] A. Lehtinen, F. Granberg, L. Laurson, K. Nordlund, M.J. Alava, Multiscale modeling of dislocation-precipitate interactions in Fe: from molecular dynamics to discrete dislocations, Phys. Rev. E 93 (2016), 013309.
[47] Y. Cui, G. Po, N. Ghoniem, Influence of loading control on strain bursts and dislocation avalanches at the nanometer and micrometer scale, Phys. Rev. B 95 (2017), 064103.
[48] Y. Cui, G. Po, N. Ghoniem, Size-tuned plastic flow localization in irradiated materials at the submicron scale, Phys. Rev. Lett. 120 (2018), 215501.
[49] G. Sparks, Y. Cui, G. Po, Q. Rizzardi, J. Marian, R. Maaβ, Avalanche statistics and the intermittent-to-smooth transition in microplasticity, Phys. Rev. Mater. 3 (2019), 080601.
[50] M. Koslowski, A. Cuitino, M. Ortiz, A phase-field theory of dislocation dynamics, strain hardening and hysteresis in ductile single crystals, J. Mech. Phys. Solids 50 (12) (2002) 2597–2635.
[51] D.W. Lee, H. Kim, A. Strachan, M. Koslowski, Effect of core energy on mobility in a continuum dislocation model, Phys. Rev. B 83 (2011), 104101.
[52] R. Groger, B. Marchand, T. Lookman, Dislocations via incompatibilities in phase-field models of microstructure evolution, Phys. Rev. B 94 (2016), 054105.
[53] H. Kim, N. Mathew, D.J. Luscher, A. Hunter, Phase field dislocation dynamics modeling of non-Schmid behavior in bcc metals informed by atomistic simulations, J. Mech. Phys. Solids 152 (2021), 104460.
[54] A. Patra, D.L. McDowell, Crystal plasticity-based constitutive modelling of irradiated bcc structures, Philos. Mag. 92 (7) (2012) 861–887.
[55] A. Tallman, L.P. Swiler, Y. Wang, D.L. McDowell, Reconciled top-down and bottom-up hierarchical multiscale calibration of bcc Fe CRYSTAL PLAsticity, Int. J. Comput. Methods Eng. 15 (6) (2017) 1–19.
[56] A.E. Tallman, L.P. Swiler, Y. Wang, D.L. McDowell, Hierarchical top-down bottom-up calibration with consideration for uncertainty and inter-scale discrepancy of peierls stress of bcc Fe, Model. Simul. Mater. Sci. Eng. 27 (2019), 064004.
[57] L. Xiong, G. Tucker, D.L. McDowell, Y. Chen, Coarse-grained atomistic simulation of dislocation, J. Mech. Phys. Solids 59 (2) (2011) 160–177.
[58] L. Xiong, D.L. McDowell, Y. Chen, Nucleation and growth of dislocation loops in Cu, Al, and Si by a concurrent atomistic-continuum method, Scr. Mater. 67 (7–8) (2012) 633–636.
[59] S. Xu, R. Che, L. Xiong, Y. Chen, D.L. McDowell, A quasistatic implementation of the concurrent atomistic-continuum method for FCC crystals, Int. J. Plast. 72 (2015) 91–126.
[60] L. Xiong, R. Ji, X. Chen, S. Xu, D.L. McDowell, Y. Chen, Coarse-grained elastodynamics of fast moving dislocations, Acta Mater. 104 (2016) 143–155.
[61] S. Xu, L. Xiong, Y. Chen, McDowell, An analysis of key characteristics of the Frank-Read Source process in FCC metals, J. Mech. Phys. Solids 96 (2016) 460–476.
[62] H. Chen, S. Xu, W. Li, R. Ji, T. Phan, L. Xiong, A spatial decomposition parallel algorithm for a concurrent atomistic-continuum simulator and its preliminary applications, Comput. Mater. Sci. 144 (2018) 1–10.
[63] S. Xu, T.G. Payne, H. Chen, Y. Liu, L. Xiong, Y. Chen, D.L. McDowell, PyCAC: the concurrent atomistic-continuum simulation environment, J. Mater. Res. 33 (7) (2018) 857–871.
[64] Y. Chen, Local stress and heat flux in atomistic systems involving three-body forces, J. Chem. Phys. 124 (5) (2006), 054113.
[65] Y. Chen, Reformulation of microscopic balance equations for multiscale materials modeling, J. Chem. Phys. 130 (13) (2009), 134706.
[66] Y. Chen, A. Diaz, Physical foundation and consistent formulation of atomic-level fluxes in transport processes, Phys. Rev. E 98 (5) (2018), 052113.
[67] Y. Chen, A. Diaz, Local momentum and heat fluxes in transient transport processes and inhomogeneous systems, Phys. Rev. E 94 (5) (2016), 053309.
[68] Y. Chen, S. Shabanov, D.L. McDowell, Concurrent atomistic-continuum modeling of crystalline materials, J. Appl. Phys. 126 (10) (2019), 101101.
[69] R. Ji, T. Phan, Y. Chen, D.L. McDowell, L. Xiong, A finite-temperature coarse-grained atomistic approach for understanding the kink-controlled dynamics of micrometer-long dislocations in high-Peierls-barrier materials, MRS Commun. 12 (2022) 1077–1085.
[70] J.G. Kirkwood, The statistical mechanical theory of transport processes II. Transport in Gases, J. Chem. Phys. 15 (1947) 72–76.
[71] J.G. Kirkwood, J.H. Irving, The statistical mechanical theory of transport processes. IV. The equations of hydrodynamics, J. Chem. Phys. 18 (1950) 817–829.
[72] J.G. Kirkwood, R.J. Bearman, Statistical mechanics of transport processes. XI. Equations of transport in multicomponent systems, J. Chem. Phys. 28 (1958) 136–145.
[73] L. Xiong, D.L. McDowell, Y. Chen, Sub-THz phonon drag on dislocations by coarse-grained atomistic simulations, Int. J. Plast. 55 (2014) 268–278.
[74] S. Xu, L. Xiong, Y. Chen, D.L. McDowell, Shear stress- and line length-dependent screw dislocation cross-slip in FCC Ni, Acta Mater. 122 (2017) 412–419.
[75] X. Chen, L. Xiong, D.L. McDowell, Y. Chen, Effects of phonons on mobility of dislocation arrays, Scr. Mater. 137 (2017) 22–26.
[76] M.C. Marinica, L. Ventelon, M.R. Gilbert, L. Proville, S.L. Dudarev, J. Marian, G. Bencteux, F. Willaime, Interatomic potentials for modelling radiation defects and dislocations in tungsten, J. Phys. Condens. Matter 25 (2013), 395502.
[77] V. Levitas, S.E. Esfahani, I. Ghamarian, Scale-free modeling of coupled evolution of discrete dislocation bands and multivariant martensitic microstructure, Phys. Rev. Lett 121 (2018), 205701.
[78] R. Gracie, T. Belytschko, Concurrently coupled atomistic and XFEM models for dislocations and cracks, Int. J. Numer. Methods Eng. 78 (2009) 354–378.
[79] A. Koester, A. Ma, A. Hartmaier, Atomistically informed crystal plasticity model for body-centered cubic iron, Acta Mater. 60 (2012) 3894–3901.
[80] E.B. Tadmor, M. Ortiz, R. Phillips, Quasicontinuum analysis of defects in solids, Philos. Mag. A 73 (1996) 1529–1563.
[81] Y. Kulkarni, J. Knap, M. Ortiz, A variational approach to coarse graining of equilibrium and non-equilibrium atomistic description at finite temperature, J. Mech. Phys. Solids 56 (4) (2008) 1417–1449.
[82] R. Meyer, L. Scherthan, T. Hochdorffer, S. Sadashivaiah, J.A. Wolny, M.W. Klein, M. Smaga, T. Beck, V. Schunemann, H.M. Urbassek, Changes in the phonon density of states of Fe induced by external strain, Appl. Phys. A 127 (2021) 5.
[83] X. Chen, A. Diaz, L. Xiong, D.L. McDowell, Y. Chen, Passing waves from atomistic to continuum, J. Comput. Phys. 354 (2018) 393–402.
[84] L. Xiong, X. Chen, N. Zhang, D.L. McDowell, Y. Chen, Prediction of phonon properties of 1D polyatomic systems using concurrent atomistic-continuum simulation, Arch. Appl. Mech. 84 (9) (2014) 1665–1675.
[85] M. Mrovec, R. Groger, A.G. Bailey, D. Nguyen-Manh, C. Elsasser, V. Vitek, Bond-order potential for simulations of extended defects in tungsten, Phys. Rev. B 75 (2007), 104119.
[86] F. Maresca, D. Dragoni, G. Csanyi, N. Marzari, W.A. Curtin, Screw dislocation structure and mobility in body centered cubic Fe predicted by a Gaussian approximation potential, npj Comput. Mater. 4 (2018) 69.
[87] A. Stukowski, Visualization and analysis of atomistic simulation data with OVITO – the open visualization tool, Model. Simul. Mater. Sci. Eng. 18 (2010), 015012.
[88] G.J. Ackland, R. Thetford, An improved N-body semi-empirical model for body-centred cubic transition metals, Philos. Mag. A 56 (1) (1987) 15–30.
[89] P.B. Hirsch, Y.Q. Sun, On the stability of the three-fold symmetrically dissociated screw dislocation in the bcc lattice, Trans. R. Soc. S. Afr. 58 (2) (2003) 129–134.
[90] D. Brunner, Comparison of flow-stress measurements on high-purity tungsten single crystals with the kink-pair theory, Mater. Trans. 41 (1) (2000) 152–160. *JIM*.
[91] A.S. Argon, S.R. Maloof, Plastic deformation of tungsten single crystals at low temperature, Acta Metall. 14 (1966) 1449–1462.
[92] M. Wen, A.H.W. Ngan, Atomistic simulation of kink-pairs of screw dislocations in body-centred cubic iron, Acta Mater. 48 (2000) 4255–4265.
[93] L. Xiong, Y. Chen, I.J. Beyerlein, D.L. McDowell, Multiscale modeling of interface-mediated mechanical, thermal, and mass transport in heterogeneous materials: perspectives and applications, J. Mater. Res. 36 (2021) 2601–2614.
[94] J. Byggmastar, A. Hamedani, K. Nordlund, F. Djurabekova, Machine-learning interatomic potential for radiation damage and defects in tungsten, Phys. Rev. B 100 (2019), 144105.
[95] A. Seeger, U. Holzwarth, Slip planes and kink properties of screw dislocations in high-purity niobium, Philos. Mag. 86 (25–26) (2006) 3861–3892.
[96] G. Schoeck, The activation energy of dislocation movement, Phys. Status Solidi 8 (1965) 499.
[97] K. Tapasa, Y.N. Osetsky, D.J. Bacon, Computer simulation of interaction of an edge dislocation with a carbon interstitial in α-iron and effects on glide, Acta Mater. 55 (2007) 93–104.
[98] Hsiung, L., 2007. Dynamic Dislocation Mechanisms For the Anomalous Slip in a Single-Crystal bcc Metal Oriented for "Single Slip''. Technical Report UCRLTR-227296 Lawrence Livermore National Laboratory Livermore, CA.
[99] D. Cereceda, M. Diehl, F. Roters, D. Raabe, J.M. Perlado, J. Marian, Unraveling the temperature dependence of the yield strength in single-crystal tungsten using atomistically-informed crystal plasticity calculations, Int. J. Plast. 78 (2016) 242–265.
[100] L. Dezerald, D. Rodney, E. Clouet, L. Ventelon, F. Willaime, Plastic anisotropy and dislocation trajectory in bcc metals, Nat. Commun. 7 (2016) 11695.
[101] A. Kraych, E. Clouet, L. Dezerald, L. Ventelon, F. Willaime, D. Rodney, Non-glide effects and dislocation core fields in bcc metals, npj Comput. Mater. 5 (2019) 109.
[102] L.M. Dupuy, E.B. Tadmor, R.E. Miller, R. Phillips, Finite-temperature quasicontinuum: molecular dynamics without all the atoms, Phys. Rev. Lett. 95 (2005), 060202.
[103] J. Marian, G. Venturini, B.L. Hansen, J. Knap, M. Ortiz, G.H. Campbell, Finite-temperature extensions of the quasicontinuum method using Langevin dynamics: entropy losses and analysis of errors, Model. Simul. Mater. Sci. Eng. 18 (2009), 015003.
[104] L. Xiong, X. Chen, N. Zhang, D.L. McDowell, Y. Chen, Prediction of phonon properties of 1D polyatomic systems using concurrent atomistic-continuum simulations, Arch. Appl. Mech. 84 (2014) 1665–1675.
[105] Chen, Y., Unifying temperature definition in atomistic and field representations of conservation laws, arXiv:2308.10127 [cond-mat.stat-mech]. (2023).